Los Alamos National Laboratory is operated by the University of California for the United States Department of Energy under contract W-7405-ENG-36.

Physics and Chemistry of Late Time Fireball Simulations Without the Geomagnetic Field

Los Alamos Los Alamos National Laboratory
Los Alamos, New Mexico 87545

This work was supported by the US Department of Energy and the Defense Nuclear Agency.

LA-11122-MS

UC-34
Issued: October 1987

Physics and Chemistry of Late Time Fireball Simulations Without the Geomagnetic Field

Eugene M. D. Symbalisty
Dale S. Sappenfield
C. Dexter Sutherland
Bryan A. Kashiwa

Los Alamos National Laboratory
Los Alamos, New Mexico 87545

PHYSICS AND CHEMISTRY OF LATE TIME FIREBALL SIMULATIONS WITHOUT THE GEOMAGNETIC FIELD

by

Eugene M. D. Symbalisty, Dale S. Sappenfield, C. Dexter Sutherland, and Bryan A. Kashiwa

ABSTRACT

This report describes the FADCAT computer code which is a version of the CAVEAT code adapted to simulate intermediate altitude fireballs. FADCAT now runs in two dimensions with all the features described herein. The three-dimensional version currently runs without the marker particles and without the Dukowicz rezone ability. We also highlight the results of two hypothetical, but realistic, burst scenarios. These are one megaton detonations: a single burst at 80 km altitude, and a double simultaneous burst at 60 and 80 km altitude.

I. INTRODUCTION

This paper describes the physics and chemistry involved in simulating the evolution of an intermediate altitude fireball that would arise from a nuclear explosion. We do not model the device in detail, and we do not start the evolution at detonation time. We assume we are given the necessary initial conditions at some time after detonation, typically one second, from an early time fireball simulator such as RADFLO or MODEL3. The link time is chosen such that it is justifiable to ignore radiation transport and energy loss altogether or to model it very simply. We also do not include the effects of the geomagnetic field. The fireball evolution is still a complicated phenomenon because of its multidimensionality and because of air chemistry. The hydrodynamic and chemical reaction time scales are such that, above some altitude, local thermodynamic equilibrium (LTE) cannot be assumed. Because chemical energy released on time scales of interest cannot be ignored, a small set of chemical rate equations must be integrated simultaneously with the hydro equations. The solution is therefore numerical. We have adapted a hydro code entitled CAVEAT developed by the theoretical hydrodynamics group at Los Alamos National Laboratory. The *F*ireball *AD*apted *CA*vea*T* is called *FADCAT*.

The code CAVEAT uses a second-order, explicit, Godunov, conservative, finite-volume scheme on an arbitrary Lagrangian-Eulerian (ALE) mesh.[1] These features provide maximum accuracy in problems of the blast wave type because an artificial viscosity is not utilized in the numerical scheme, and the mesh can follow the fluid motion over a large part of the problem simulation. Additionally, the CAVEAT code is designed to make optimum use of the vector processing feature of modern supercomputers. This means that very fast, accurate solutions to the multidimensional Euler equations are relatively easy to obtain.

II. INITIAL CONDITIONS AND THE AMBIENT ATMOSPHERE

The procedure for starting a problem evolution is to (1) establish a computational grid, (2) establish an ambient atmosphere on the grid, (3) stabilize the atmosphere, and (4) replace the ambient values with the early time interface values within the region that the early time interface values are defined. When we are simulating an historic event, we set up an ambient atmosphere as close to what is known for that event. This may include as information the CIRA atmosphere for that date and time, and/or rocket sounding data. For example, for the Fishbowl series of atmospheric tests we have defined a Fishbowl atmosphere. When we are simulating a hypothetical burst, then we use what we have defined as a mean atmosphere.

The mean atmosphere is based on the U.S. Standard Atmosphere, 1962[2] and the CIRA 1965[3] atmosphere. Above 120 km the CIRA Model 5 (mean solar activity) hour 8 (*average* over the 24-hour variation) is used. Figures 1.1 and 1.2 display the altitude variations in density, local scale height, pressure, and temperature for the mean atmosphere. The Fishbowl atmosphere comes from the same sources. Above 120 km the CIRA Model 2 (low solar activity, believed to be appropriate in 1962) hour 0 (near shot times) is used.

The ambient atmosphere must then be stabilized on the grid so that if there were no explosion there would be no motion. The acceleration due to gravity is defined at cell centers. In hydrostatic equilibrium, we have

$$\nabla p = \rho g \tag{1.1}$$

where the gradient is derived between cell faces, so that it is a cell centered quantity as well. FADCAT obtains cell face pressures, necessary for the gradient, from the Riemann solver. The internal energy (and hence temperature and pressure) is adjusted so that Equation 1.1 is satisfied with the calculated face centered Riemann pressures. Since the gradient operator is defined over multiple cells, the adjustment is made from the top of the grid to the bottom via a Newton-Raphson iteration. If the cell sizes are much less than a local scale height, then the adjustment is very small, typically less than one percent. If the cell sizes are comparable to a scale height, then the energy adjustments may be as large as ten percent. We have chosen to adjust e instead of ρ because we feel it is more important to preserve the mass distribution surrounding the burst point instead of the temperature distribution.

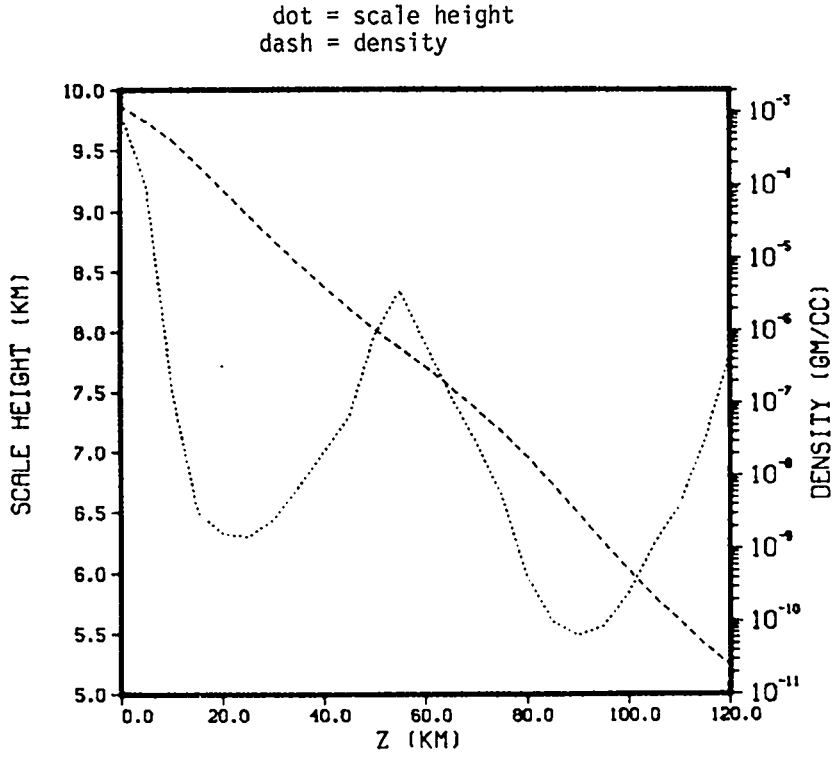

Fig. 1.1. The local scale height (dot) and mass density (dash) as a function of altitude in the MEANAIR atmosphere.

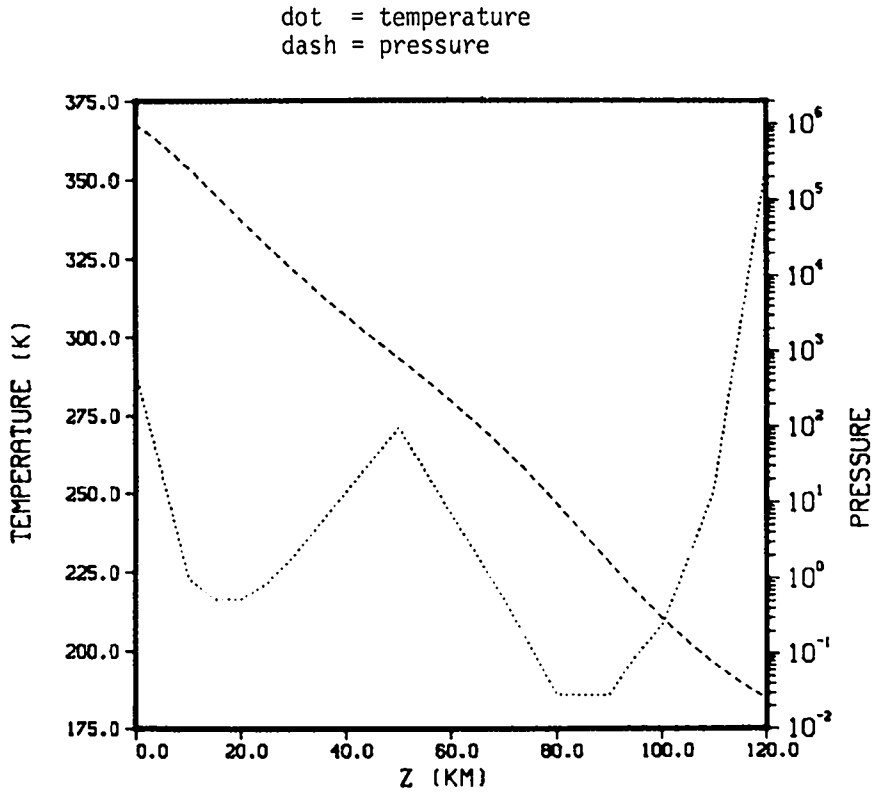

Fig. 1.2. The temperature (dot) and pressure (dash) as a function of altitude in the MEANAIR atmosphere.

The replacement of the ambient values with the early time initial conditions from RADFLO[20] or MODEL3 is straightforward. Because MODEL3 carries many more ionized species than FADCAT it is necessary to recombine multiply-charged atomic ions into singly-charged ions, and to represent the sum of molecular ion densities as a single molecular ion density. Replacement of ambient quantities with quantities from a RADFLO calculation is more involved because RADFLO, being an equilibrium code, does not carry individual chemical species. The chemical species needed by FADCAT can be determined from temperature, total density, and the equilibrium tables of Gilmore.[6] However, care must be taken not to change the total internal energy, and some adjustment of the interpolated chemical species densities is usually necessary.

III. THE LTE EQUATIONS

Every atmospheric fireball will rise due to buoyancy and pressure forces. Pressure will also push the ambient air surrounding the detonation point down, but because ambient density and pressure decrease with altitude, the upward motion will be enhanced and the downward motion damped. There exists a yield of device, for a given altitude, below which the disturbed atmosphere will not reach an altitude where chemical reaction time scales are slow enough to demand a non-LTE description of the gas. Therefore there exists a yield-altitude range where LTE is valid. In this case the LTE equations are the Euler equations. We list them here:

$$\frac{\partial \rho}{\partial t} + \nabla \bullet (\rho \mathbf{u}) = 0 \tag{2.1}$$

$$\frac{\partial (\rho \mathbf{u})}{\partial t} + \nabla \bullet (\rho \mathbf{u}\mathbf{u}) = -\nabla p + \rho \mathbf{g}$$

$$\frac{\partial (\rho E)}{\partial t} + \nabla \bullet (\rho E \mathbf{u}) = -\nabla \bullet (p\mathbf{u}) + \rho \mathbf{g} \bullet \mathbf{u}$$

$$e = E - \frac{\mathbf{u} \bullet \mathbf{u}}{2}$$

The symbol **u** is the velocity field, p is the pressure, **g** the gravitational acceleration, ρ is the mass density, e is the specific internal energy, and E is the specific total energy.

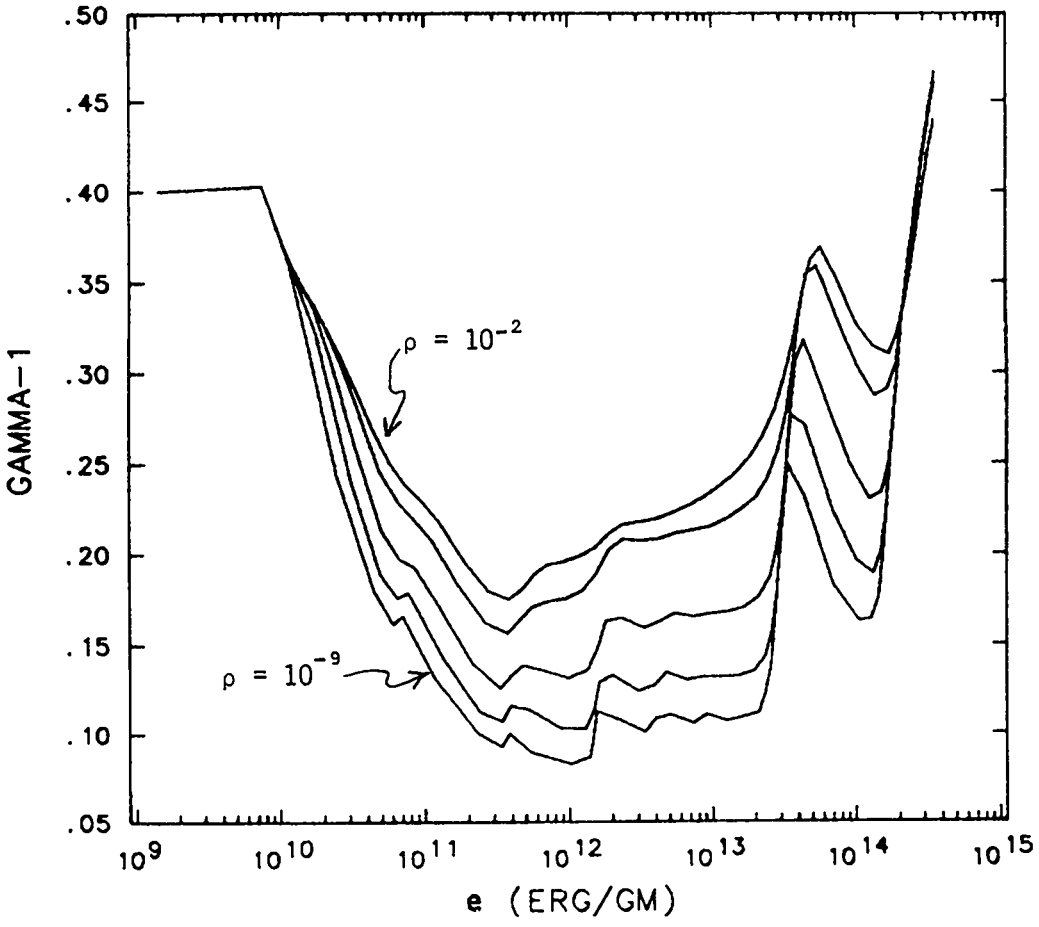

Fig. 2.1. The $\gamma - 1$ of air vs. specific internal energy (e) for a series of density values, according to the EOS used in LTE calculations. The density values are $10^{-2}, 10^{-3}, 10^{-5}, 10^{-7}, 10^{-9}$.

The procedure for solving Eq. (2.1) belongs to the class of numerical methods called control volume techniques. CAVEAT uses an ALE control volume method wherein the problem domain is overlaid by a mesh, dividing the domain into a succession of adjacent control volumes called cells. The integral form of Eq. (2.1) is then applied to each cell of the mesh, so that the physical laws of conservation are satisfied in each control volume. The corners of each cell are allowed to move according to a prescribed velocity. This *mesh* velocity can be the *Lagrangian* velocity, an *adaptive* velocity based on the mesh generator equations or any linear combination thereof, including zero. In the problems described here a best estimate of the Lagrangian fluid velocity at the cell vertices is used to move the mesh. When the mesh becomes excessively distorted, the computation is stopped momentarily and the mesh is rezoned to a regular configuration using the conservative rezoning scheme of Dukowicz [7]. This practice minimizes errors due to arbitrary fluid-mesh relative motion (called Eulerian diffusion).

We need only to specify an equation of state (EOS), $p(\rho, e)$, to complete the set of equations. We use an EOS for air based on equation of state tables of Hilsenrath et al[4,5] and Gilmore[6]. The range of validity is 1000 K to 5×10^6 K, based on the tables. Extrapolation beyond this range is straightforward. In terms of density, the tables are valid for $1.29 \times 10^{-9} < \rho < 1.29 \times 10^{-2}$. The net result is that the EOS will return an effective γ and T when given ρ and e. The pressure is then $p = (\gamma - 1)\rho e$. Figure 2.1 plots $\gamma - 1$ as a function of e for different values of ρ. Figure 2.2 plots T as a function of e for the same values of ρ.

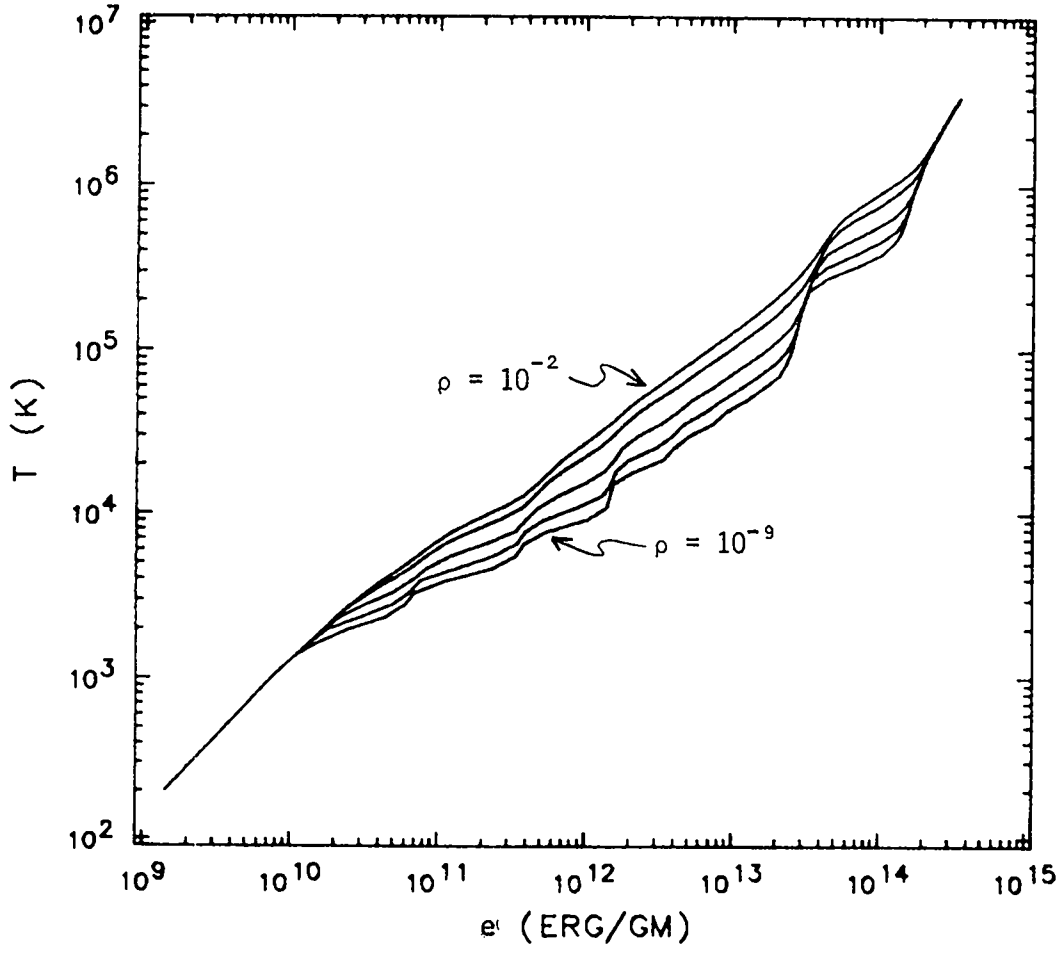

Fig. 2.2. The temperature of air vs. e for the same series of densities as in Figure 2.1, according to the LTE EOS.

The control-volume numerical scheme used in CAVEAT is distinguished from most other methods by its use of coincident control volumes for mass and momentum. Classical ALE techniques use a staggered configuration in which the momentum control volumes are centered on the vertices of the mass control volumes. The particular form of the discretized integral equations used in CAVEAT is a second-order variant of Godunov's method. In Godunov's method each cell is thought of as a slab of material adjoining other material slabs with different initial conditions of pressure, density, and velocity. The cell side is then considered a contact surface moving in space with a continuous velocity and pressure that can be determined by solution of the so-called Riemann problem [8]. CAVEAT uses the approximate Riemann solver introduced by Dukowicz [8] to provide the cell side pressure and the cell side normal velocity needed in the control volume integration. These cell side quantities effectively contain the viscosity needed to provide sufficient entropy increase in shock waves, but no more than is physically present as dictated by the nature of the materials involved. This minimizes the number of cells over which discontinuities in the flow are resolved.

IV. THE NON-LTE EQUATIONS

The equation of mass conservation is replaced by equations of number conservation,

$$\frac{\partial n_i}{\partial t} + \nabla \bullet (n_i \mathbf{u}) = S_i \tag{3.1}$$

where each specie, n_i , has the same velocity field, $\mathbf{u}$. S_i is the change in n_i due to chemical reactions. The mass density is now a derived quantity and is calculated as

$$\rho = \sum n_i m_i \tag{3.2}$$

where m_i is the atomic mass of specie (i).

The equation of momentum conservation, with the above definition of ρ, is identical to the LTE equation:

$$\frac{\partial(\rho \mathbf{u})}{\partial t} + \nabla \bullet (\rho \mathbf{u}\mathbf{u}) = -\nabla p + \rho \mathbf{g} \quad . \tag{3.3}$$

We note that chemistry is absent from the momentum equation because the reaction network is allowed to change internal energy only and not momenta. The pressure is calculated as before

$$p = (\gamma - 1)\rho e \tag{3.4}$$

but where

$$\gamma - 1 = \frac{S_m + S_a + n_e}{2.5S_m + 1.5(S_a + n_e)}$$

and

$$S_m = \sum molecular\ concentrations$$

$$S_a = \sum atomic\ concentrations$$

n_e is the electron density which is identical to the ion density. e is limited to energy in translation and rotation. The factor 2.5 in front of the molecule sum is due to the fact that all the molecules that we evolve are diatomic. We could alternatively set $p = (\sum n_i)kT$, because the temperature, T, is necessary for the chemistry. We choose to calculate a local gamma for the gas because it plays a role in the Riemann solver in the hydro code. We also note that we have neglected viscosity.

The equation for specific total energy, E, (translation, rotation, and kinetic) is the LTE equation with a heat source, Q,

$$\frac{\partial(\rho E)}{\partial t} + \nabla \bullet (\rho E \mathbf{u}) = -\nabla \bullet (p\mathbf{u}) + \rho \mathbf{g} \bullet \mathbf{u} + Q \tag{3.5}$$

Q is the energy release/absorption rate per unit volume and is exactly the opposite of the change in the chemical energy per unit volume energy. Therefore energy is conserved exactly.

We evolve the number densities $N_2, N, N^+, O_2, O, O^+, NO, NO^+$ and sometimes He. Helium is included for problems that reach very high altitude where it is the dominant ambient constituent of the atmosphere. Helium only enters the reaction network as a source for the three-body reactions. The chemical energy is the sum of ionizational, dissociational, and vibrational energies. The ionization energy is

$$I(ev/cc) = 9.267[NO^+] + 13.618[O^+] + 14.534[N^+] \quad . \tag{3.6}$$

The dissociation energy is

$$D(ev/cc) = 4.880([N] + [N^+]) + 2.558([O] + [O^+]) + 0.931([NO] + [NO^+]) \quad . \tag{3.7}$$

The vibrational energy is calculated from the temperature as follows

$$V(ev/molecule) = \frac{0.3e^{-0.3/T}}{1. - e^{-0.3/T}} \tag{3.8}$$

where T is the temperature in ev. Equation 3.8 is derived by assuming the vibrational energy levels are

$$E_{v,i} = i0.3\ eV,\ \ i = 1, \infty$$

and the population of each level is

$$N_{v,i} = n_o e^{-E_{v,i}/T} \quad .$$

The following energy sum is unchanged, for each Lagrangian volume element as well as globally, by the chemistry model

$$\rho e + S_m V + I + D = constant \tag{3.9}$$

and since the kinetic and gravitational energies are untouched by the chemistry model, the total energy remains constant as well. The above equation defines Q, the change in material energy due to chemistry, as

$$Q = -\frac{\delta(S_m V + I + D)}{\delta t} \tag{3.10}$$

The symbol δ is used here to denote the difference between the value at the beginning and the end of the chemistry calculation. The temperature is defined implicitly in the following equation:

$$\rho e + (S_m V)_o = (1.5(S_a + n_e) + 2.5S_m)T + S_m V(T) \tag{3.11}$$

which is solved for T by a Newton-Raphson iteration. In Equation 3.11 we have assumed that NO, O_2, and NO^+ vibrational energies are similar to N_2 vibrational energy, which was estimated by Equation 3.8. Also in equation (3.11) $(S_m V)_o$ is the vibrational energy entering the chemistry model.

A. Chemistry Model

It can easily be shown that local thermodynamic equilibrium cannot be assumed to exist with respect to chemical species concentrations during the evolution of an intermediate altitude fireball. Furthermore, the energy that is initially tied up in the form of chemical energy cannot be assumed to be unimportant. For example, at 1 second the energy in ionization in the Kingfish fireball is computed to be approximately 25 percent of the energy in translation and rotation. The rate at which chemical energy is converted to thermal energy must be taken into account in the calculation of fireball expansion and rise. The composition of the air in the fireball must be known in order to compute pressure.

These considerations dictate that some chemical calculation must be coupled to the hydrodynamic calculation performed by FADCAT. It is not necessary to do a complete chemistry calculation, as one needs to do to predict all optical/infrared radiation from the fireball (assuming that the amount of energy radiated is negligible). A calculation that follows the concentrations of the major species that determine pressure and contain most of the chemical energy should be adequate. We have determined that the following species need to be included in the in-line chemistry: $N_2, N(^4S), N^+(^3P), O_2, O(^3P), O^+(^4S), NO$, and NO^+. Free-electron density is the sum of the ion densities. Inclusion of $N(^2D)$ was considered, but for the Kingfish calculation $N(^2D)$ does not appear to be necessary. It may be required for calculations at lower altitude.

Our initial approach to in-line chemistry for FADCAT was straightforward numerical integration of a coupled set of rate equations using the GEAR technique. Computational times were found to be prohibitive. Alternatives that were considered included performing chemical computations on a subset of a FADCAT grid, using a faster predictor-corrector integration technique, and advancing the chemical species concentrations by analytic integration of decoupled rate equations. The third alternative was chosen because it was considered the best compromise among accuracy, speed, and predictable computational time. Because the rate equations are decoupled one does have to demonstrate that acceptable accuracy can be achieved. After describing the integration sequence we will compare results of the integrations performed with the decoupled equations with results given by the fully coupled GEAR technique.[16] The chemical reactions will be presented in groups, in the order in which the reactions are integrated. An alternative would be to vary the integration order from time step to time step.

REACTION GROUP 1

$$N^+ + 2e \leftrightarrow N + e \qquad (a)$$

$$0^+ + 2e \leftrightarrow O + e \qquad (b.1)$$

$$N^+ + O \rightarrow O^+ + N \qquad (b.2)$$

The direction of reactions (a) and (b.1) depends on whether the electron density is greater than or less than an approximate equilibrium value. The equilibrium value is computed with the equation

$$\frac{{n_e}^2}{\sum[N_i] + \sum[O_i] - n_e} = f(T) \qquad (3.12)$$

in which n_e is electron density (assumed equal to $[N^+] + [O^+]$), $\sum[N_i]$ and $\sum[O_i]$ are the sums of neutral and singly ionized atomic nitrogen and oxygen, respectively, and

$$f(T) = 6.02 \times 10^{21} \mathrm{T}^{3/2} \exp(-\bar{\mathrm{E}}/\mathrm{t}). \qquad (3.13)$$

In Equation (3.13) T is temperature in eV and $\bar{\mathrm{E}}$ is the density-weighted mean ionization potential of nitrogen and oxygen. Electron density associated with NO^+ is ignored. If NO^+ is present in significant quantities it is unlikely that collisional-radiative recombination or electron-atom ionization is important.

If n_e is less than the value computed with Eq. (3.12) reactions (a) and (b) are treated as ionization reactions. The rate equation is

$$\dot{n_e} = k([N] + [O])n_e, \qquad (3.14)$$

in which $[N]$ and $[O]$ are the time-dependent nitrogen and oxygen atom densities. The rate constant, k, is computed as

$$k = \frac{[N]_o 4.72 \times 10^{-9} T^{0.755} exp(-14.123/T) + [O]_o 9.85 \times 10^{-9} T^{0.597} exp(-13.518/T)}{[N]_o + [O]_o}, \qquad (3.15)$$

in which $[N]_o$ and $[O]_o$ are the nitrogen and oxygen atom densities at the beginning of the integration time step. The ionization rate constants are fits to the rate constants given by Lotz [9]. The integration can be done analytically, with k constant over the time step. Changes in $[N], [N^+], [O]$, and $[O^+]$ are proportional to the individual rate constants embedded in Eq. (3.15).

If n_e is greater than the value given by Eq. (3.12) reactions (a) and (b.1) are treated as recombination reactions. The rate equation is

$$\dot{n_e} = -k([N^+] + [O^+])n_e \tag{3.16}$$

in which $[N^+]$ and $[O^+]$ are the time-dependent nitrogen and oxygen atomic ion densities. The rate constant is based on detailed calculations of collisional-radiative recombination rate constants. Values of the rate constant are given in Tables 3.1 and 3.2 [10] and are plotted in Figures 3.1 and 3.2. A weighted average rate constant, computed in a way analogous to Eq. (3.15), is used in Eq. (3.16).

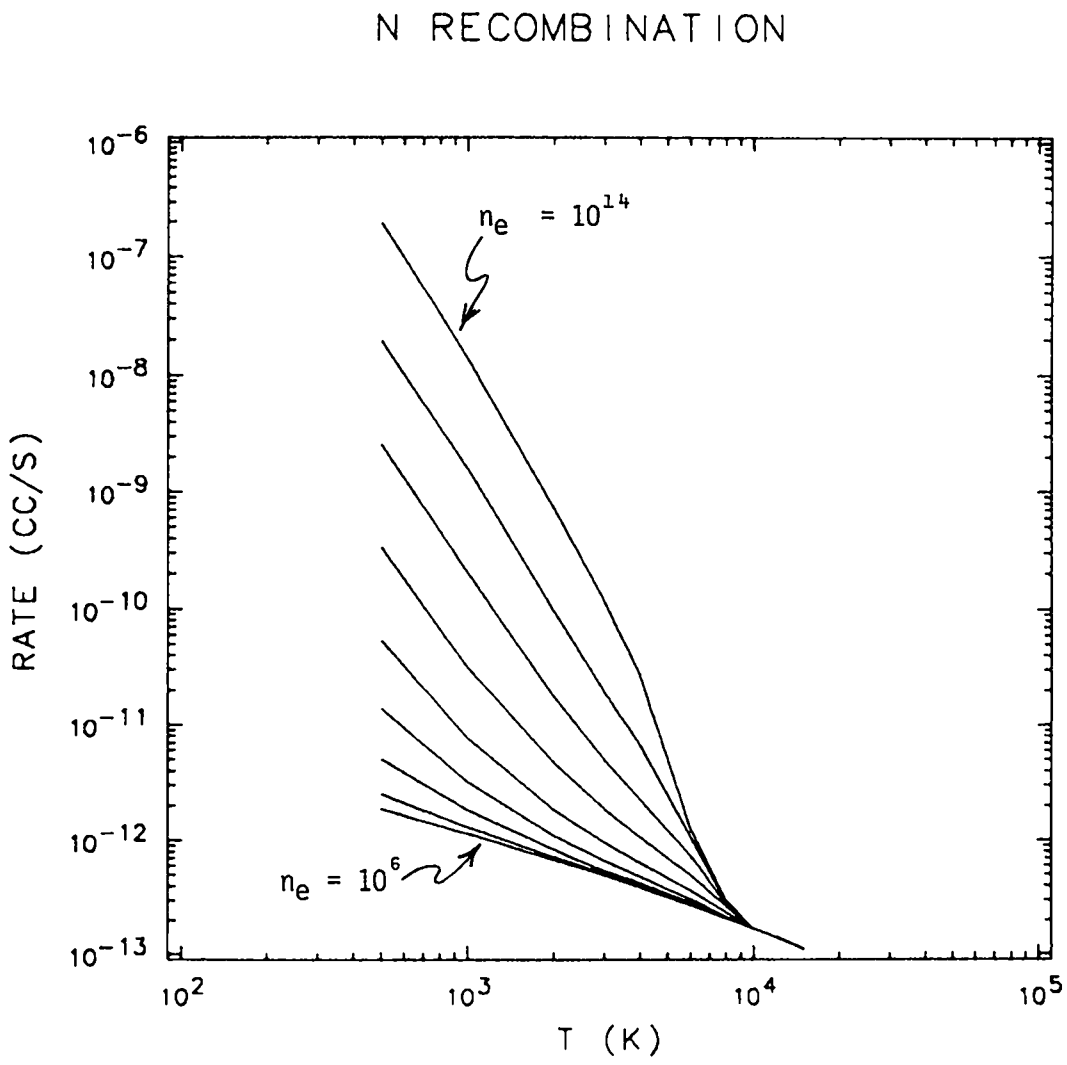

Fig. 3.1. The nitrogen recombination rate constant for nine values of electron density. These are $n_e = 10^6, 10^7, 10^8, 10^9, 10^{10}, 10^{11}, 10^{12}, 10^{13}, 10^{14}$.

The integration is done analytically. Changes in $[N], [N^+], [O]$, and $[O^+]$ are proportional to $[N^+]_o$ and $[O^+]_o$.

Electron-ion recombination can produce radiation, which in principle can be as large as the ionization potential plus the kinetic energy of the recombining electron. At intermediate altitudes the mean free path of a photon that can be absorbed by the ground term of the atom is very short, so that at most only photons generated in transitions to excited terms can escape from the disturbed volume. Energy lost by radiation then

TABLE 3.1. Collisional-Radiative Recombination Rate Constants (cm^3/s) For Nitrogen Electron Density (cm^{-3})

Temperature	Electron Density (cm^{-3})								
(K)	1.0E+06	1.0E+07	1.0E+08	1.0E+09	1.0E+10	1.0E+11	1.0E+12	1.0E+13	1.0E+14
500.	1.90E-12	2.50E-12	5.00E-12	1.38E-11	5.37E-11	3.33E-10	2.52E-09	1.95E-08	1.94E-07
1000.	1.15E-12	1.31E-12	1.83E-12	3.17E-12	7.58E-12	3.09E-11	2.01E-10	1.56E-09	1.36E-08
2000.	6.81E-13	7.19E-13	8.36E-13	1.10E-12	1.84E-12	4.66E-12	1.75E-11	9.56E-11	7.17E-10
3000.	4.93E-13	5.09E-13	5.58E-13	6.67E-13	9.59E-13	1.88E-12	5.01E-12	1.94E-11	1.16E-10
4000.	3.88E-13	3.97E-13	4.22E-13	4.81E-13	6.34E-13	1.07E-12	2.27E-12	6.79E-12	2.72E-11
6000.	2.71E-13	2.73E-13	2.83E-13	3.06E-13	3.64E-13	4.98E-13	7.46E-13	1.10E-12	1.32E-12
8000.	2.08E-13	2.08E-13	2.08E-13	2.12E-13	2.33E-13	2.63E-13	2.76E-13	2.89E-13	3.02E-13
10000.	1.68E-13	1.68E-13	1.68E-13	1.68E-13	1.68E-13	1.68E-13	1.68E-13	1.68E-13	1.68E-13
12000.	1.41E-13	1.41E-13	1.41E-13	1.41E-13	1.41E-13	1.41E-13	1.41E-13	1.41E-13	1.41E-13
15000.	1.12E-13	1.12E-13	1.12E-13	1.12E-13	1.12E-13	1.12E-13	1.12E-13	1.12E-13	1.12E-13

TABLE 3.2. Collisional-Radiative Recombination Rate Constants (cm^3/s) For Oxygen Electron Density (cm^{-3})

Temperature	Electron Density (cm^{-3})								
(K)	1.0E+06	1.0E+07	1.0E+08	1.0E+09	1.0E+10	1.0E+11	1.0E+12	1.0E+13	1.0E+14
500.	2.20E-12	4.06E-12	9.30E-12	2.66E-11	1.08E-10	6.58E-10	4.76E-09	3.70E-08	3.67E-07
1000.	1.18E-12	1.63E-12	2.59E-12	4.83E-12	1.18E-11	4.22E-11	2.28E-10	1.64E-09	1.40E-08
2000.	6.43E-13	7.58E-13	9.72E-13	1.37E-12	2.30E-12	5.04E-12	1.60E-11	7.65E-11	5.21E-10
3000.	4.49E-13	5.02E-13	5.94E-13	7.53E-13	1.08E-12	1.89E-12	4.50E-12	1.56E-11	8.47E-11
4000.	3.47E-13	3.77E-13	4.28E-13	5.11E-13	6.70E-13	1.03E-12	2.05E-12	5.78E-12	2.51E-11
6000.	2.37E-13	2.51E-13	2.73E-13	3.06E-13	3.64E-13	4.83E-13	7.64E-13	1.56E-12	3.55E-12
8000.	1.77E-13	1.85E-13	1.97E-13	2.13E-13	2.39E-13	2.87E-13	3.86E-13	5.50E-13	7.10E-13
10000.	1.42E-13	1.42E-13	1.48E-13	1.56E-13	1.68E-13	1.86E-13	2.14E-13	2.32E-13	2.50E-13
12000.	1.18E-13	1.18E-13	1.18E-13	1.18E-13	1.21E-13	1.25E-13	1.29E-13	1.33E-13	1.37E-13
15000.	9.36E-14	9.36E-14	9.36E-14	9.36E-14	9.36E-14	9.36E-14	9.36E-14	9.36E-14	9.36E-14

is about 25% of the ionization potential, plus the kinetic energy of the recombining electron, which is usually small by comparison. It is possible that even less energy will be radiated, because of quenching of excited terms.

The calculations reported here and elsewhere are done with the assumption that 25% of the ionization potential is lost by radiation after each electron-ion recombination, and that the remaining 75 % of the ionization potential is returned as thermal energy.

Reaction (b.2) can affect the overall deionization rate because the oxygen ion can react with molecular nitrogen whereas the nitrogen ion cannot. In general, the region within which molecular oxygen is destroyed is larger than the region in which molecular nitrogen is destroyed, so that without reaction (b.2) nitrogen ions could survive in a larger volume.

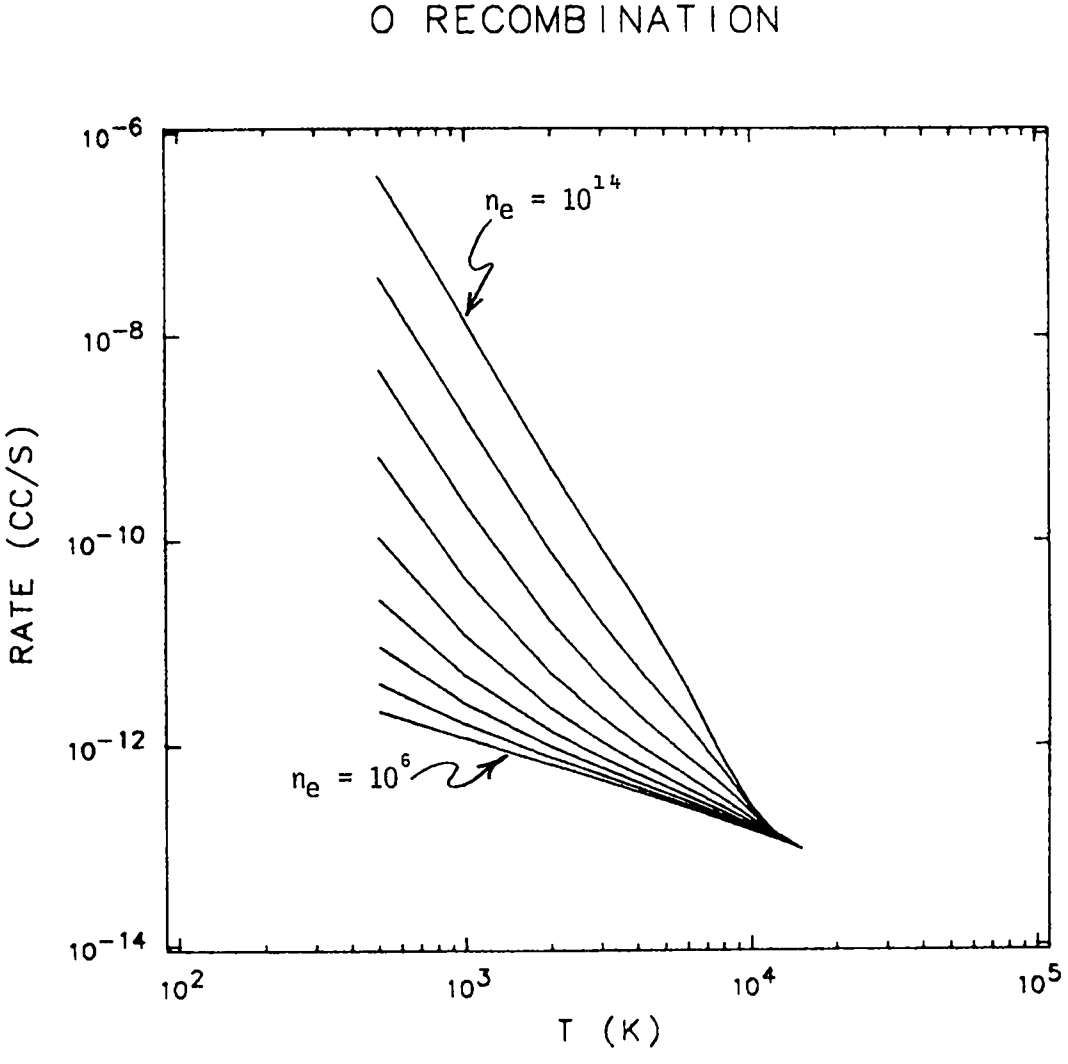

Fig. 3.2. The oxygen recombination rate constant for the same nine values of electron density in Figure 3.1.

The rate constant for reaction (b.2) has been measured at ion energies well above 1 eV. The only indication of which we are aware of the rate constant at lower temperatures comes from an inference from nuclear test data by Scheibe and Kaufman (private communication). Their inference of a lower limit to the rate constant is 1.0×10^{-12} *cc/s*. We have used a value twice that, only for consistency with other calculations.

Reaction (b.2) is computed only when recombination is occurring.

Because the rate constants in Eqs. (3.14) and (3.16) are held constant over an integration time step, and because reactions (a) and (b) can consume or release large amounts of energy, it is sometimes necessary to limit the reaction time step to a value that is smaller than the FADCAT time step. One repeats the chemical integration time step until the FADCAT time step is completed. The condition on the reaction time step is that the fractional change in internal energy caused by the chemical reaction be less than 0.075. For the

Kingfish problem Reaction Group 1 is the only reaction group for which it is sometimes necessary to take a smaller reaction time step than is imposed by FADCAT. For lower altitude explosions time steps taken for other reaction groups may also need to be limited.

REACTION GROUP 2

$$N^+ + O_2 \rightarrow NO^+ + O \qquad (c)$$

$$O^+ + N_2 \rightarrow NO^+ + N \qquad (d)$$

These two reactions are independent and are integrated independently. The rate equations are

$$[\dot{N^+}] = -k[N^+][O_2], \quad k = 2.8 \times 10^{-10} cm^3/s \quad [11] \qquad (3.17)$$

and

$$[\dot{O^+}] = -k[O^+][N_2]. \qquad (3.18)$$

For reaction (d) the rate constant is $3 \times 10^{-14}/T$ for $T < 0.0646$, and $1.2 \times 10^{-10}T^2$ for $T \geq 0.0646$.[12] The temperature is limited to $0.02 \leq T \leq 1.0$ eV.

REACTION GROUP 3

$$O^+ + O_2 \rightarrow {O_2}^+ + O \qquad (e)$$

This reaction is included to provide a faster reaction path for destruction of O^+ than would exist via reaction (d) in cold air. In heated air (but with molecules still present) reaction (d) will be faster.

The rate equation is similar to Eq. (3.18) with $k = 2.2 \times 10^{-11} cm^3/s$.[11] Because ${O_2}^+$ is needed only as a product of this reaction it is not carried explicitly as a species in the chemistry routine. For computational purposes the product is assumed to NO^+. This can be rationalized either by assuming prompt charge exchange between ${O_2}^+$ and NO, or by transmutation.

REACTION GROUP 4

$$NO^+ + e \leftrightarrow N + O \qquad (f)$$

The rate equation is

$$[\dot{NO^+}] = k_1[N][O] - k_2[NO^+]n_e, \qquad (3.19)$$

$k_1 = 1.7 \times 10^{-11}T^{0.6}exp(-2.76/T)$,[13] and $k_2 = 9.27 \times 10^{-8}T^{-0.4} cm^3/s$.[11] In integrating Eq. (3.19) we do include electron density attributable to N^+ and O^+, as well as to NO^+. The integration is still analytic.

REACTION GROUP 5

$$N + O_2 \rightarrow NO + O, \; k_1 = 4.4 \times 10^{-12}exp(-0.277/T), \quad [14] \qquad (g)$$

$$N + NO \rightarrow N_2 + O, \; k_2 = 3.4 \times 10^{-11} \quad [14] \qquad (h)$$

Reactions (g) and (h) are combined to give a quasi-steady NO density. The main purpose of including these reactions is to provide under some circumstances a faster path for N-atom recombination than 3-body recombination.

The NO density is first adjusted to its quasi-steady value, defined as

$$[NO] = \frac{k_1}{k_2}\,[O_2], \qquad (3.20)$$

$[N]$, $[O]$ and $[O_2]$ being adjusted if $[NO]$ must be produced, (the changes in $[NO]$ and $[O_2]$ being treated self-consistently) $[N]$, $[O]$ and $[N_2]$ being adjusted if $[NO]$ must be destroyed. Then, under the assumption that reaction (g) is rate-limiting, destruction of N atoms during the integration interval is computed with the rate equation

$$[\dot{N}] = -2\, k_1[N][O_2] \tag{3.21}$$

The changes in $[N]$ and $[O_2]$ are computed explicitly. The change in $[NO]$ is computed with Eq. (3.20). The changes in $[N_2]$ and $[O]$ are computed from conservation of nitrogen and oxygen atoms.

REACTION GROUP 6

$$N + O + M \rightarrow NO + M,\ k = 1.60 \times 10^{-33}/T^{\frac{1}{2}} \quad [11] \tag{i}$$

This reaction is included only if the quasi-steady NO density resulting from its use with reaction (h) is greater than the the quasi-steady density given by Eq. (3.20). In most cases Eq. (3.20) gives the larger density. Because recombination of N atoms has already been computed via Eq. (3.21) this reaction is used only to increase NO to the larger, quasi-steady value. If reaction (i) were often the dominant reaction for NO production the logic used for reaction groups 5 and 6 would have to be changed.

REACTION GROUP 7

$$2N + M \leftrightarrow N_2 + M, \tag{j}$$

$$k_f = 8.3 \times 10^{-34} exp(0.0431/T), \quad k_r = 1.9 \times^{-9} T^{-1.6} exp(-9.76/T); \quad [15]$$

and

$$2O + M \leftrightarrow O_2 + M, \tag{k}$$

$$k_f = 3.4 \times 10^{-34}/T, \quad k_r = 8.7 \times 10^{-10} T^{-1.5} exp(-5.12/T). \quad [15]$$

The rate equation for reaction (j) is

$$[\dot{N}] = -2k_f[N]^2[M] + 2k_r[N_2][M] \tag{3.22}$$

the rate equation for reaction (k) is analogous.

B. Tests of the Chemistry Integration

Results given by the sequential, analytic integration scheme have been checked against results given by numerical integration of the same rate equations with the same rate constants. The numerical integration of the rate equations is done by the subroutine SDRVB3 in the Common Los Alamos Mathematical Software. The subroutine is written by D.K. Kahaner and C. D. Sutherland, and uses the GEAR integration technique.[16] In the numerical solution all rate equations are fully coupled.

For these comparisons we have altered the treatment of Reaction Group 1 so that both ionization and recombination rates are integrated, without regard to the equilibrium ionization. We make this modification because it is difficult to impose the equilibrium condition on the numerical integrator.

We have made comparisons for three sets of initial species densities, which are representative of weakly disturbed, moderately disturbed, and strongly disturbed conditions at 90 km altitude. For each set of species densities we use two initial temperatures, giving us a total of six test cases.

The sequential, analytic integration is intended to run in-line with a hydrodynamic calculation. The hydrodynamics will superimpose temperature (and also density) changes on top of the temperature changes produced by changes in chemical energy. Without running a hydrodynamic calculation we cannot incorporate hydrodynamically induced temperature and density changes into our test problems. Rather, we make simplifying assumptions with respect to both density and temperature. The total mass density is held constant in all cases. One set of comparisons is made with temperature also held constant. Another set of comparisons is made with the temperature allowed to change in response to change in chemical energy.

TABLE 3.3. Initial Species Densities[a] and Temperatures[b]

	Case 1	Case 2	Case 3
$[N_2]$	4.9×10^{13}	3.53×10^{13}	6.10^{11}
[N]	2×10^{12}	2×10^{13}	5×10^{13}
$[N^+]$	1×10^{11}	5×10^{12}	5×10^{13}
$[O_2]$	1.21×10^{13}	7.43×10^{12}	2×10^{11}
[O]	2×10^{12}	6×10^{12}	1.33×10^{13}
$[O^+]$	1×10^{11}	1×10^{12}	1.33×10^{13}
[NO]	0	0	0
$[NO^+]$	5×10^{11}	5×10^{12}	0
[e-]	7×10^{11}	1.1×10^{13}	6.33×10^{13}
Temperature 1	0.043	0.173	0.517
Temperature 2	0.086	0.345	0.345

[a] cm^{-3}
[b] eV

These cases may bound many real cases. For example, if chemical energy is being released, temperature will rise. However, the gas will probably respond by expanding, both reducing the net temperature rise and slowing the rate of chemical reactions.

The initial species densities and temperatures are shown in Table 3.3.

Results of the comparisons are shown in Tables 3.4 and 3.5 . The result of primary interest is chemical energy, the change in which (less radiation losses, if any) is the energy added to or subtracted from the thermal energy. We also show comparisons of computed electron density.

To compute temperature from thermal energy, and *vice versa*, we assume that the N_2 vibrational states are populated in equilibrium, and we ignore vibrational excitation of O_2, NO, and NO^+.

The comparisons between numerical and sequential-analytic integrations at constant temperature are considered satisfactory. The differences in temperature in Cases 2 and 3 that occur when temperature is allowed to vary can be traced to differences in the rates of recombination of N_2 via Reaction Group 5. The sequential-analytic integration of Reaction Group 5 will be re-examined, because this Reaction Group can be expected to be more important at lower altitudes than it is at Kingfish altitude.

V. RESULTS

In order to gain confidence in our intermediate altitude fireball model (i.e. FADCAT) we must compare our numerical solutions to analytic and/or experimental results. This is an ongoing process. Analytic results do not exist for realistic bursts. However, since a fireball is, crudely speaking, a shock ball, then it makes sense to test CAVEAT with 1-D shock problems where analytical results exist. The results of two test problems have been documented in Addessio et al.[1] and Dukowicz[8]. The first problem is an infinitely strong shock wave propagating into a stratified gamma law gas. The second problem is the spherical Noh problem solved on a cylindrical mesh. We do not reproduce the results from these test problems here, but only mention that the agreement between numerical and analytic solution is excellent.

The best test of FADCAT is comparison with experiment. There were four historic events that can be used as test cases[17]. These include two events from the 1958 HARDTACK test series in the Pacific ocean - Teak (at 76 km altitude) and Orange (at 43 km altitude). The other two events are from the 1962 FISHBOWL test series - Kingfish and Bluegill. Kingfish and Teak have been simulated on FADCAT. The analysis of the numerical results is classified and is to be documented elsewhere.

We report here the results of two realistic, hypothetical events. The first event is the detonation of a 1 MT device at 80 km altitude. The second event is the simultaneous detonation of two 1 MT devices, one at 80 km altitude and the other 20 km directly below it at 60 km altitude. In each case FADCAT started at one second, having interfaced with an early time fireball simulator at this time. MODEL3 was the early time simulator for event 1 and event 2 combined this output with the RADFLO-2D output of a 1 MT device at 60 km.

In order to give a flavor for the initial conditions we plot in Figures 4.1.a–c isotherms at one second for 1 MT at 60, event 1, and event 2. Further analysis and description of the initial conditions will be detailed

TABLE 3.4. Comparisons of Numerical and Sequential Analytic Integrations at Constant Temperature

		Chemical Energy		$[e^-]$	
Case/Time	Temperature	(num)	(S-A)	(num)	(S-A)
Case 1					
0.0 s	0.043 eV	2.3×10^{13} eV/cm^3	2.3×10^{13}	7.0×10^{11}	7.0×10^{11}
0.001		2.1×10^{13}	2.1×10^{13}	7.4×10^{10}	6.6×10^{10}
1.0		1.9×10^{13}	2.0×10^{13}	3.0×10^{6}	3.1×10^{6}
10.0		1.6×10^{13}	2.1×10^{13}	3.1×10^{5}	3.1×10^{5}
0.0 s	0.086	2.3×10^{13}	2.3×10^{13}	7.0×10^{11}	7.0×10^{11}
0.001		2.1×10^{13}	2.1×10^{13}	7.7×10^{10}	7.6×10^{10}
1.0		1.5×10^{13}	2.1×10^{13}	4.0×10^{6}	4.1×10^{6}
10.0		1.4×10^{13}	2.1×10^{13}	4.0×10^{5}	4.0×10^{5}
Case 2					
0.0 s	0.173 eV	2.8×10^{14}	2.8×10^{14}	1.1×10^{13}	1.1×10^{13}
0.001		2.2×10^{14}	2.1×10^{14}	1.8×10^{12}	1.4×10^{12}
1.0		2.0×10^{14}	1.9×10^{14}	5.0×10^{7}	4.5×10^{7}
10.0		2.0×10^{14}	1.9×10^{14}	5.0×10^{7}	4.5×10^{7}
0.0	0.345	2.8×10^{14}	2.8×10^{14}	1.1×10^{13}	1.1×10^{13}
0.001		2.2×10^{14}	2.2×10^{14}	1.8×10^{12}	1.7×10^{12}
1.0		2.0×10^{14}	2.0×10^{14}	3.9×10^{9}	3.7×10^{9}
10.0		2.0×10^{14}	2.0×10^{14}	3.9×10^{9}	4.0×10^{9}
Case 3					
0.0 s	0.345 eV	1.3×10^{15}	1.3×10^{15}	6.3×10^{13}	6.3×10^{13}
0.001		1.0×10^{15}	1.0×10^{15}	3.2×10^{13}	3.1×10^{13}
1.0		5.7×10^{14}	5.6×10^{14}	4.4×10^{11}	3.3×10^{11}
10.0		5.6×10^{14}	5.6×10^{14}	7.9×10^{10}	7.0×10^{10}
0.0	0.517	1.3×10^{15}	1.3×10^{15}	6.3×10^{13}	6.3×10^{13}
0.001		1.3×10^{15}	1.4×10^{15}	5.4×10^{13}	5.7×10^{13}
1.0		5.8×10^{14}	5.7×10^{14}	1.0×10^{12}	8.5×10^{11}
10.0		5.6×10^{14}	5.6×10^{14}	1.5×10^{11}	1.6×10^{11}

elsewhere. In each of these figures if there were no bursts the isotherms would be exactly horizontal reflecting the ambient temperature variation with altitude. The isotherms in Figures 4.1.a and 4.1.b are not exactly circular because the energy deposition covers an altitude range larger than an atmospheric scale height, due to the thin air at these altitudes. For example the smallest contour plotted in Figure 4.1.a (0.05 eV or 580 K) extends 6.8 km downward, 8.1 km radially, and 10.2 km upward from the burst point. Figure 4.1.b shows an even greater asymmetry.

Figure 4.1.c also displays why the axisymmetric 2-burst problem was separated by 20 km. The chosen separation is so that only the relatively lower temperature isotherms intersect, and hence the overlapping interaction region is relatively small. Therefore we can expect that our 2-burst initial conditions, derived from the output from 2 separate codes on 2 separate meshes combined onto a third mesh, will be fairly realistic. We could have separated the bursts even further, in fact to the point where a region of unperturbed atmosphere existed between them. However if we had done that then the two evolving fireballs would not interact until a much later time.

TABLE 3.5. Comparisons of Numeric and Sequential Analytic Integration with Variable Temperature

	Temperature (eV)		Chemical Energy (eV/cm^3)		$[e^-]$	
Case/Time	(Num)	(S-A)	(Num)	(S-A)	(Num)	(S-A)
Case 1						
0	0.043	0.043	2.3×10^{13}	2.3×10^{13}	7.0×10^{11}	7.0×10^{11}
0.001	0.058	0.058	2.1×10^{13}	2.1×10^{13}	7.7×10^{10}	6.8×10^{10}
1.0	0.095	0.058	1.5×10^{13}	2.1×10^{13}	3.9×10^{6}	4.2×10^{5}
10.0	0.096	0.058	1.4×10^{13}	2.1×10^{13}	4.2×10^{5}	4.2×10^{5}
0	0.086	0.086	2.3×10^{13}	2.3×10^{13}	7.0×10^{11}	7.0×10^{11}
0.001	0.010	0.101	2.1×10^{13}	2.1×10^{13}	7.7×10^{10}	7.1×10^{10}
1.0	0.134	0.100	1.4×10^{13}	2.1×10^{13}	4.8×10^{6}	5.2×10^{6}
10.0	0.134	0.100	1.4×10^{13}	2.1×10^{13}	4.8×10^{5}	5.2×10^{5}
Case 2						
0	0.173	0.173	2.8×10^{14}	2.8×10^{14}	1.1×10^{13}	1.1×10^{13}
0.001	0.42	0.43	2.2×10^{14}	2.2×10^{14}	1.7×10^{12}	1.7×10^{12}
1.0	0.52	0.45	2.0×10^{14}	2.2×10^{14}	1.8×10^{10}	2.5×10^{10}
10.0	0.49	0.40	2.1×10^{14}	2.3×10^{14}	1.6×10^{10}	1.7×10^{10}
0	0.345	0.345	2.8×10^{14}	2.8×10^{14}	1.1×10^{13}	1.1×10^{13}
0.001	0.59	0.59	2.2×10^{14}	2.2×10^{14}	1.5×10^{12}	1.5×10^{12}
1.0	0.58	0.47	2.2×10^{14}	2.5×10^{14}	3.0×10^{10}	3.2×10^{10}
10.0	0.50	0.41	2.4×10^{14}	2.6×10^{14}	2.1×10^{10}	2.1×10^{10}
Case 3						
0	0.345	0.345	1.5×10^{15}	1.5×10^{15}	6.3×10^{13}	6.3×10^{13}
0.001	0.68	0.55	1.3×10^{15}	1.4×10^{15}	5.5×10^{13}	5.7×10^{13}
1.0	1.2	1.2	1.2×10^{15}	1.2×10^{15}	4.6×10^{13}	4.5×10^{13}
10.0	1.2	1.2	1.2×10^{15}	1.2×10^{15}	4.6×10^{13}	4.5×10^{13}
0	0.517	0.517	1.5×10^{15}	1.5×10^{15}	6.3×10^{13}	6.3×10^{13}
0.001	0.69	0.52	1.4×10^{15}	1.4×10^{15}	5.7×10^{13}	6.0×10^{13}
1.0	1.2	1.2	1.2×10^{15}	1.2×10^{15}	4.7×10^{13}	4.7×10^{13}
10.0	1.2	1.2	1.2×10^{15}	1.2×10^{15}	4.7×10^{13}	4.7×10^{13}

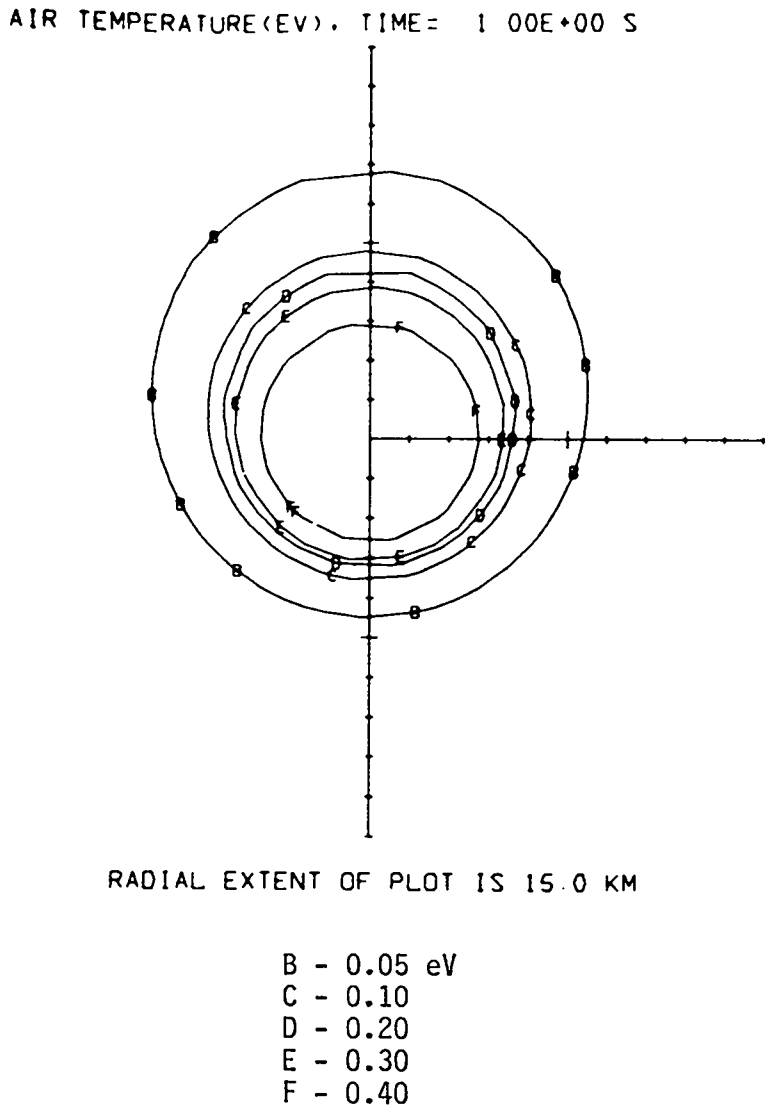

Fig. 4.1.a. The air temperature distribution in eV, at 1 second, of the air surrounding a 1 MT burst at 60 km. The early time fireball simulator for this case was RADFLO-2D.

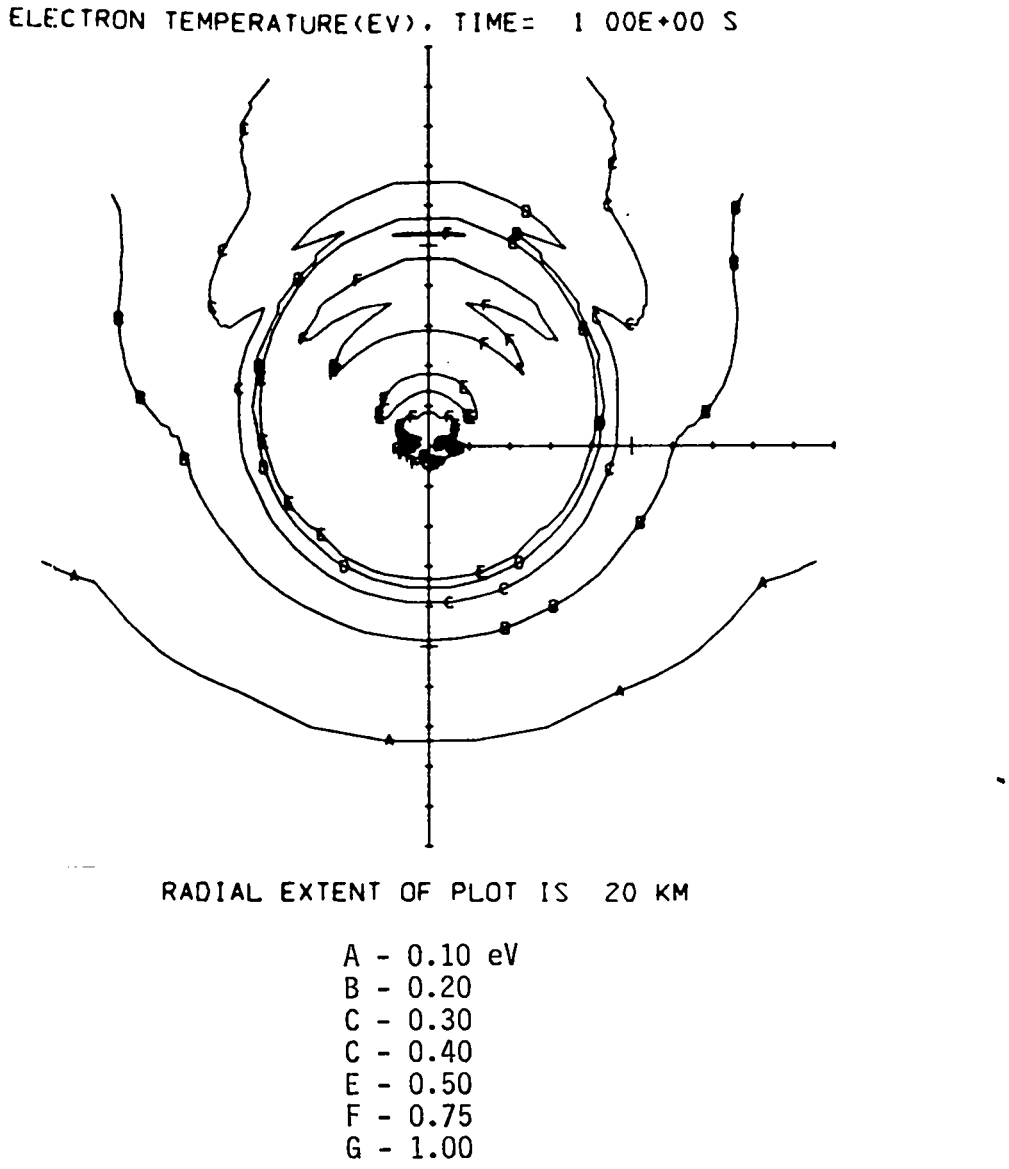

Fig. 4.1.b. The electron temperature distribution in eV, at 1 second, of the air surrounding a 1 MT burst at 80 km. The early time fireball simulator for this case was MODEL3.

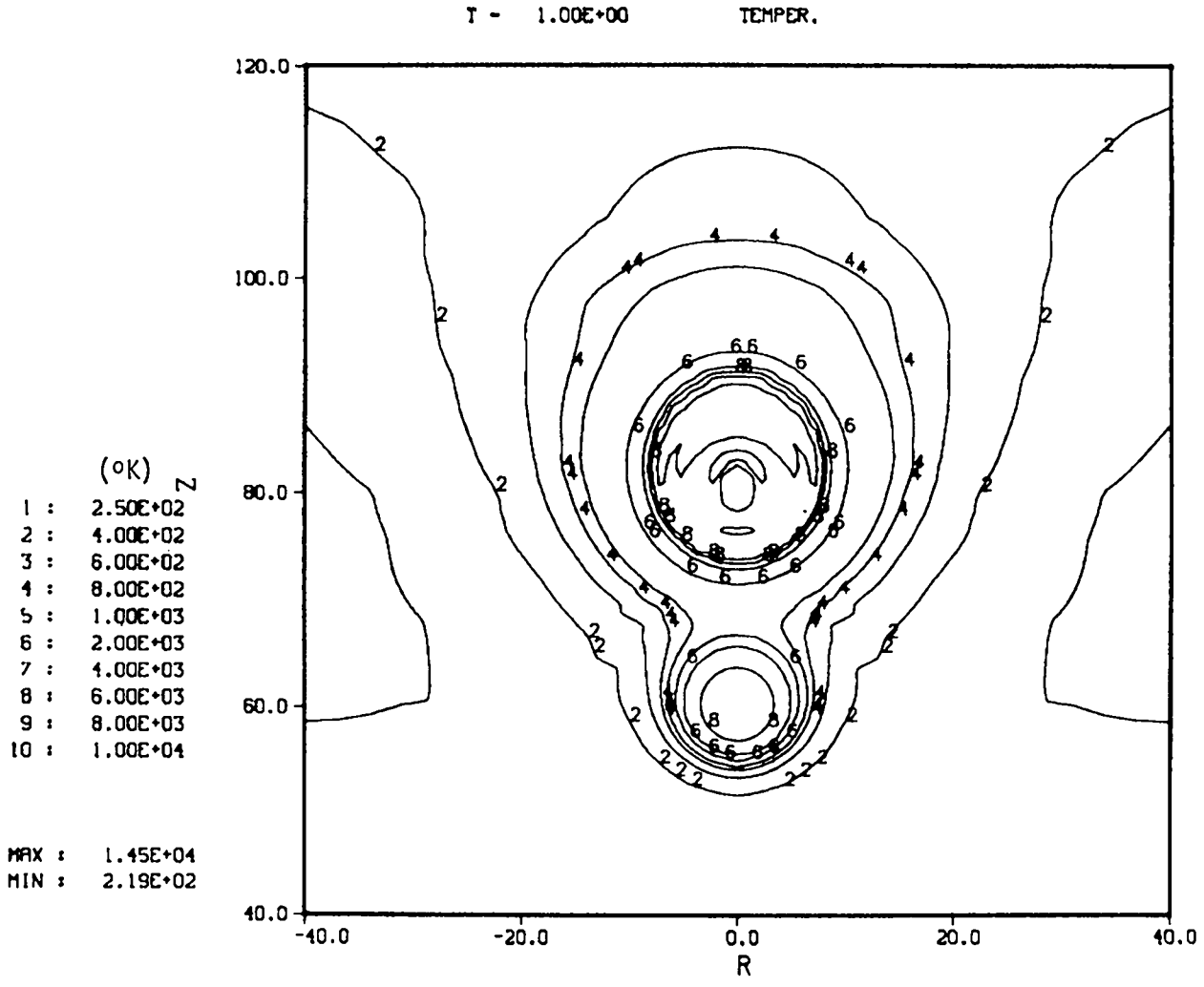

Fig. 4.1.c. The air temperature distribution in K, at 1 second, of the air surrounding the two simultaneous 1 MT bursts in event 2. The two detonations at 60 and 80 km are clearly visible.

We are now confronted with the problem of how to display or describe or analyze an enormous amount of numerical output. We will report here on what we feel are the highlights. We can always go back and extend the analysis because we have saved a series of numerical data dumps. Perhaps the most obvious feature of fireball evolution is the shock front. At early times the shock front is smeared out and becomes much sharper as time evolves. Figures 4.2.a,b plot the position of the shock top and bottom and the maximum horizontal radius, respectively, from 2 to 30 seconds for both of the hypothetical events. There are several interesting features. The shock top for event 1 (the 1 MT at 80 km) and for event 2 (the 1 MT at 80 and at 60 km) start at identical positions. This is certainly reasonable, since as we have seen from the isotherms in Figure 1, the lower burst does not disturb the air above the 80 km burst to any large extent. We also see from Figure 4.2a that the shock tops of the two events track nearly the same path. The shock top positions give roughly a uniform velocity, after 10 seconds, of 3.85 km/s and 3.95 km/s for events 1 and 2 respectively. These numbers, differing by less than 3 per cent, may be equivalent to within grid resolution. Each calculation was run on a computational grid of 50 horizontal by 100 vertical zones. This is relatively crude zoning but was deemed adequate for these hypothetical events. The zoning was finer in event 1 because it did not require as much vertical space. Event 1 required 1783 computational cycles to reach 30 seconds from the 1 second starting time. This gives an average time step of 16.3 ms. Event 2 required 1835 cycles which gives an average time step of 15.8 ms. Both events were simulated in a purely Lagrangian mode with an occasional remap to an orthogonal, time dependent, quadrilateral grid. Both events were rezoned every second from 2 to 15 seconds and every two seconds thereafter which gives a total of 21 rezones. Hence, on average, a rezone occurred every 80-90 cycles.

solid - 1 MT at 80 km and 1 MT at 60 km
dash - 1 MT at 80 km only

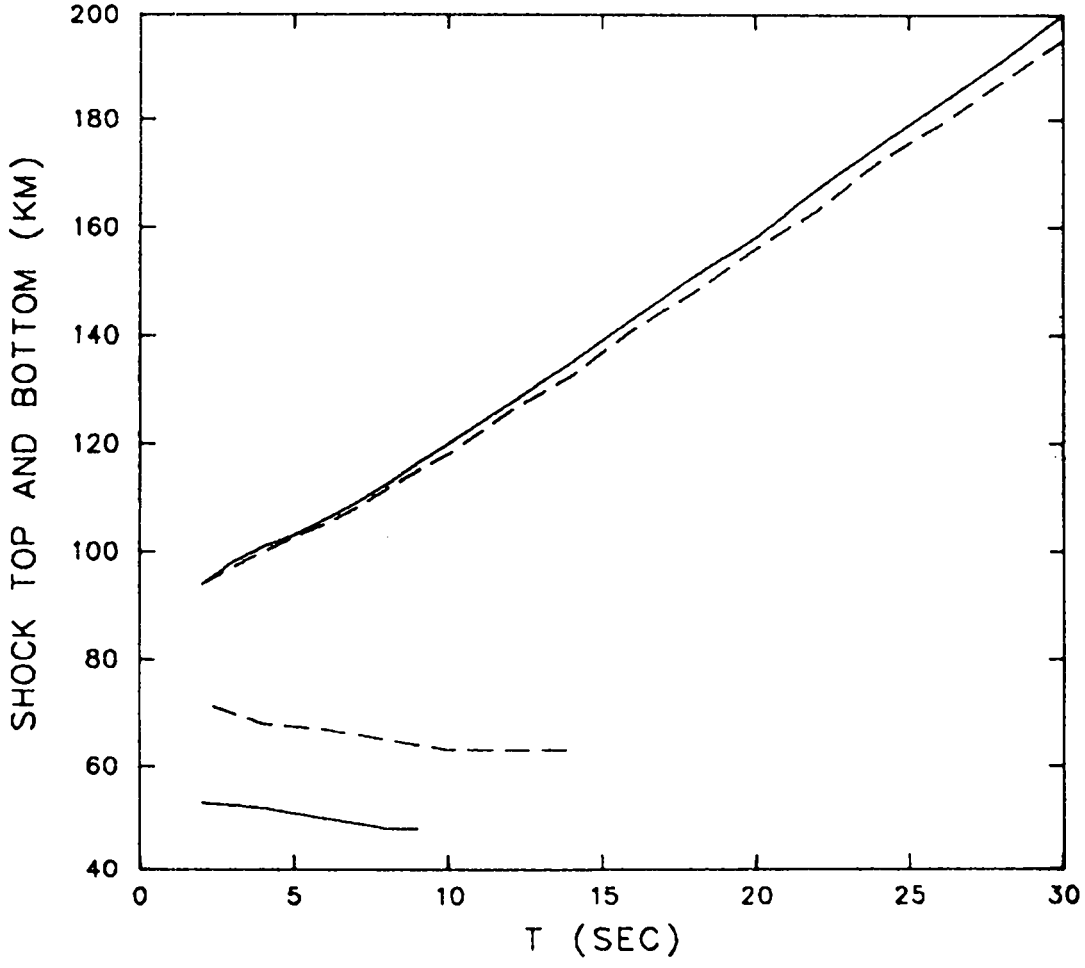

Fig. 4.2.a. The time evolution of the shock top and bottom for events 1 (dash) and 2 (solid).

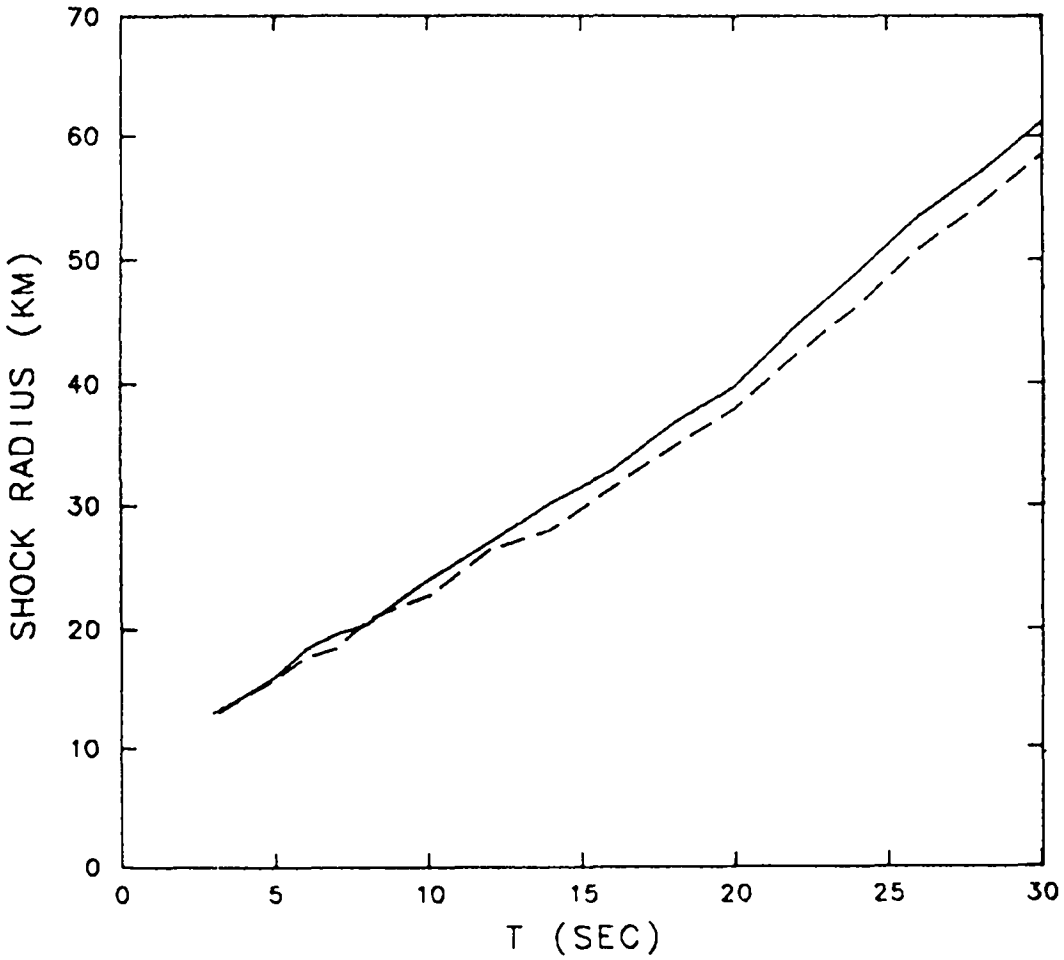

Fig. 4.2.b. The time evolution of the maximum shock horizontal radius for events 1 (dash) and 2 (solid).

The downward propagating shock of event 2 starts about 20 km below the downward propagating shock of event 1 for the obvious reason that the second burst in event 2 was 20 km below the single burst of event 1. Both bottom shocks are damped to the point of being indistinguishable from the ambient atmosphere by 15 seconds. The damping is due to the shock propagating into a denser medium. It is still possible that a sound wave is propagating down and in fact all the way to the ground. We do not track this possibility. In fact, a loud boom was heard by observers on board ship during the Kingfish and Bluegill tests.

The maximum horizontal radii (Figure 4.2.b) start at the same points for the 2 events and again track very similar paths. The altitude at which the maximum radius occurs is time dependent. It takes about 20 seconds before a roughly constant maximum radius velocity is established to be compared to the 10 seconds for the shock top velocity. After 20 seconds the maximum shock radius velocity is 2.1 km/s for both events. The main conclusion to be drawn from studying the shock evolution is that the lower burst in event 2 only affects the position of the bottom shock which dies by 15 seconds.

Figures 4.3.a,b also support this conclusion. Each figure displays isotherms at 30s in the evolution. The temperature distribution for event 2 at 1 second (Figure 4.1.c) clearly delineates the two bursts. However, at 30 seconds the shock envelopes as outlined by the isotherms in Figures 4.3.a (event 2) and 4.3.b (event 1) are very similar. The temperature distribution within the shock envelopes still is different, and one can clearly see the remnant of the lower burst in event 2 in Figure 4.3.a.

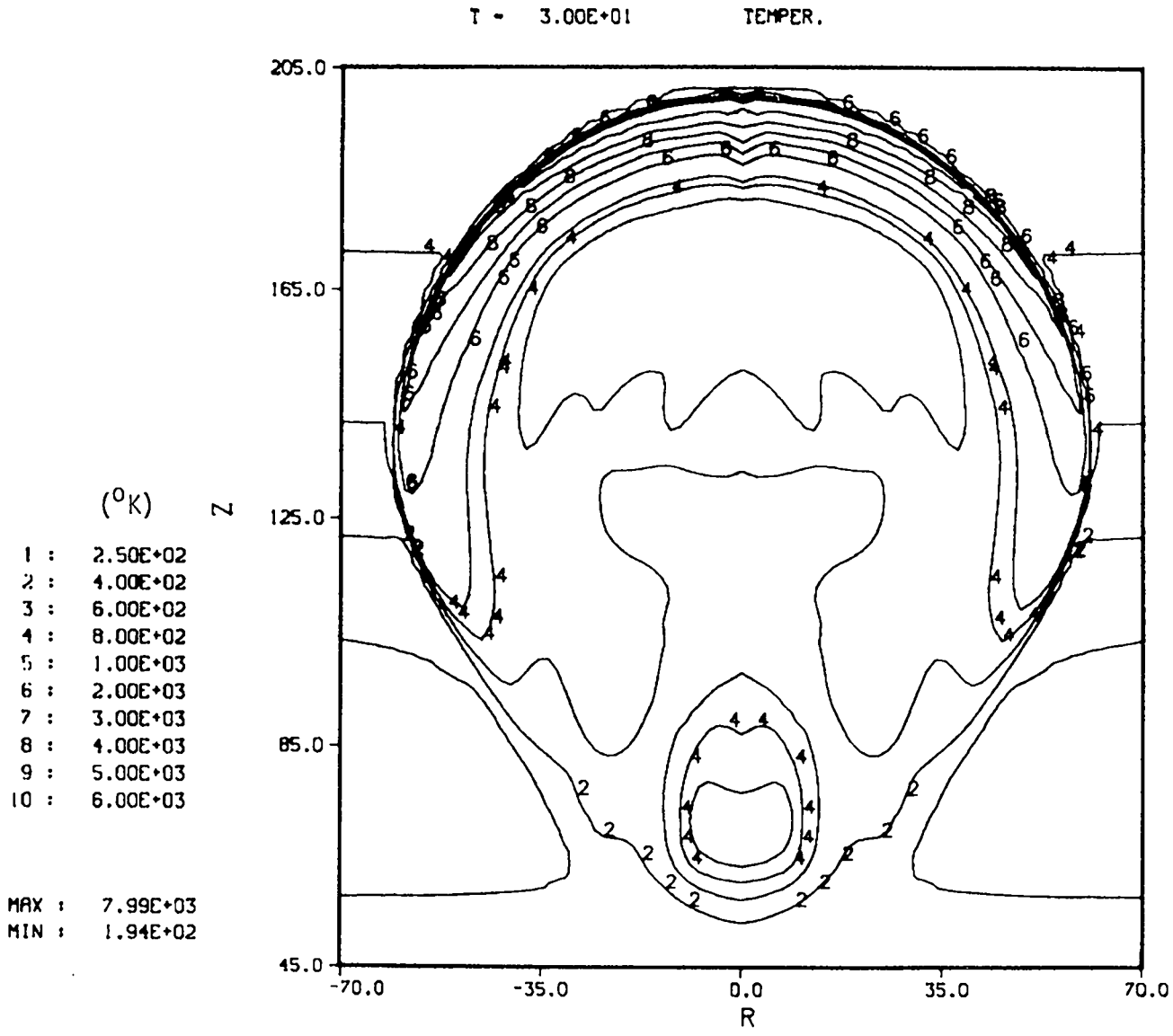

Fig. 4.3.a. Isotherms for event 2 at 30s. The shock envelope would suggest that only 1 burst occurred (see Figure 4.3.b), but the temperature distribution shows the effect of the lower burst inside the shock envelope.

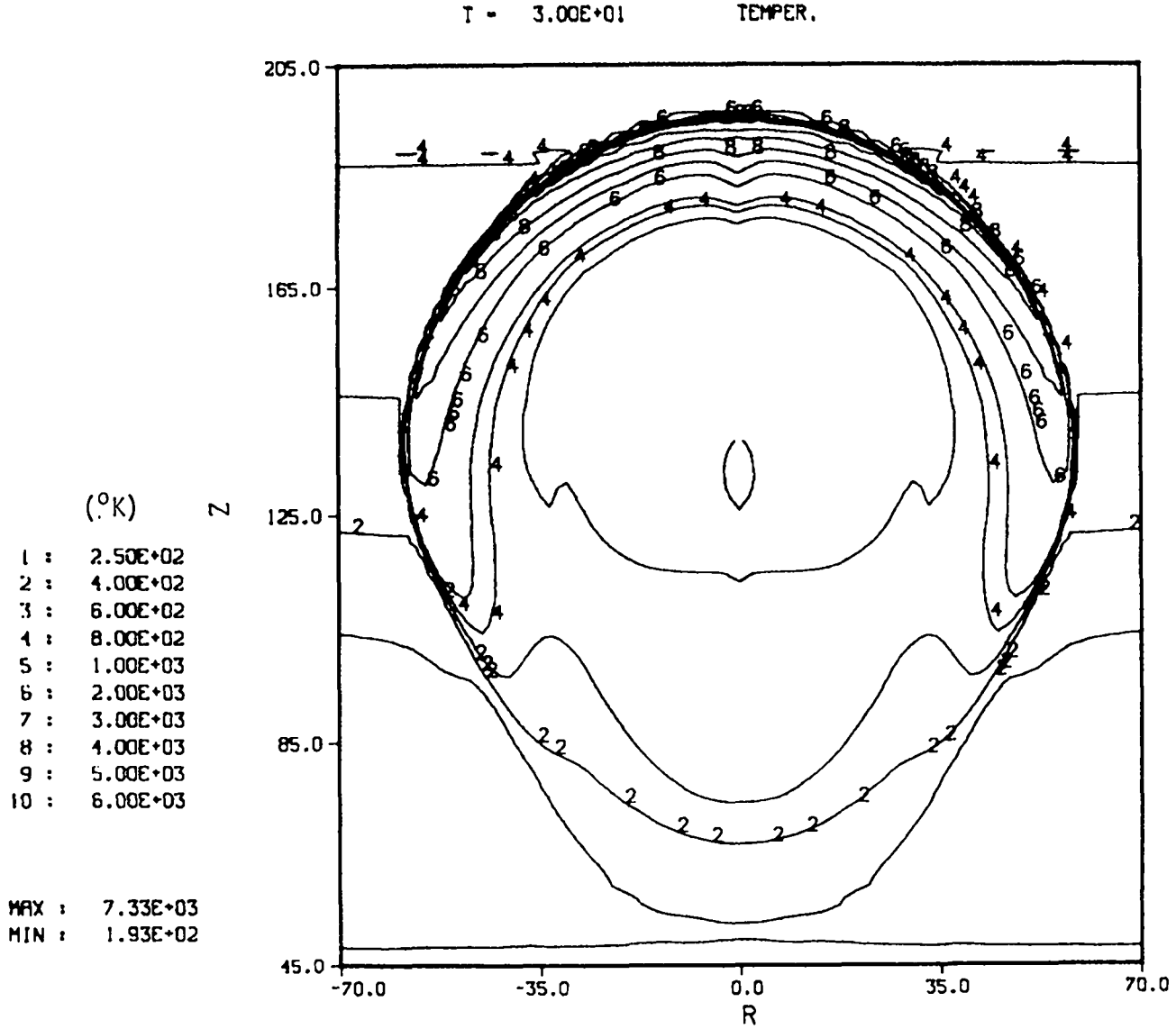

Fig. 4.3.b. Isotherms for event 1 at 30s. The grid scales and the values of the isotherms plotted are identical to Figure 4.3.a.

The electron (or ion) density distribution is an important property because electrons and ions are usually associated with emission processes. The ambient atmosphere contains few or no electrons/ions at intermediate altitude. The detonation of a nuclear device immediately creates a great deal of ionization. The ionized atmosphere then relaxes back to a neutral state because of various chemical reactions (see section 3). Figure 4.4 plots the number of ions in the computational grid for events 1 and 2 from 2 to 30 seconds. The two curves are very similar in shape with event 2 starting with a greater number of ions. However, contours of constant electron density (Figures 4.5.a,b) show the effect of the lower burst. Event 2 (see Figure 4.5.a) shows three distinct regions of high electron concentration. (We note that if one chose to plot lower contour levels then the three regions would all be encompassed by a curve of a lower electron concentration). Event 1 (Figure 4.5.b) only shows two regions of high electron concentration. The lower burst maintains a low altitude region of relatively high electron concentration near the lower burst point of 60 km. The electron concentrations in this region range from one to ten million per cc. Also the bottom of the middle region of event 2 is squashed by the lower burst. We also note that the electron/ion concentrations can be very sensitive to the chemistry model. We found, while debugging the chemistry model, that it is quite possible to change the electron distribution significantly without changing the position of the shock envelope.

solid - 1 MT at 80 km and 1 MT at 60 km
dash - 1 MT at 80 km only

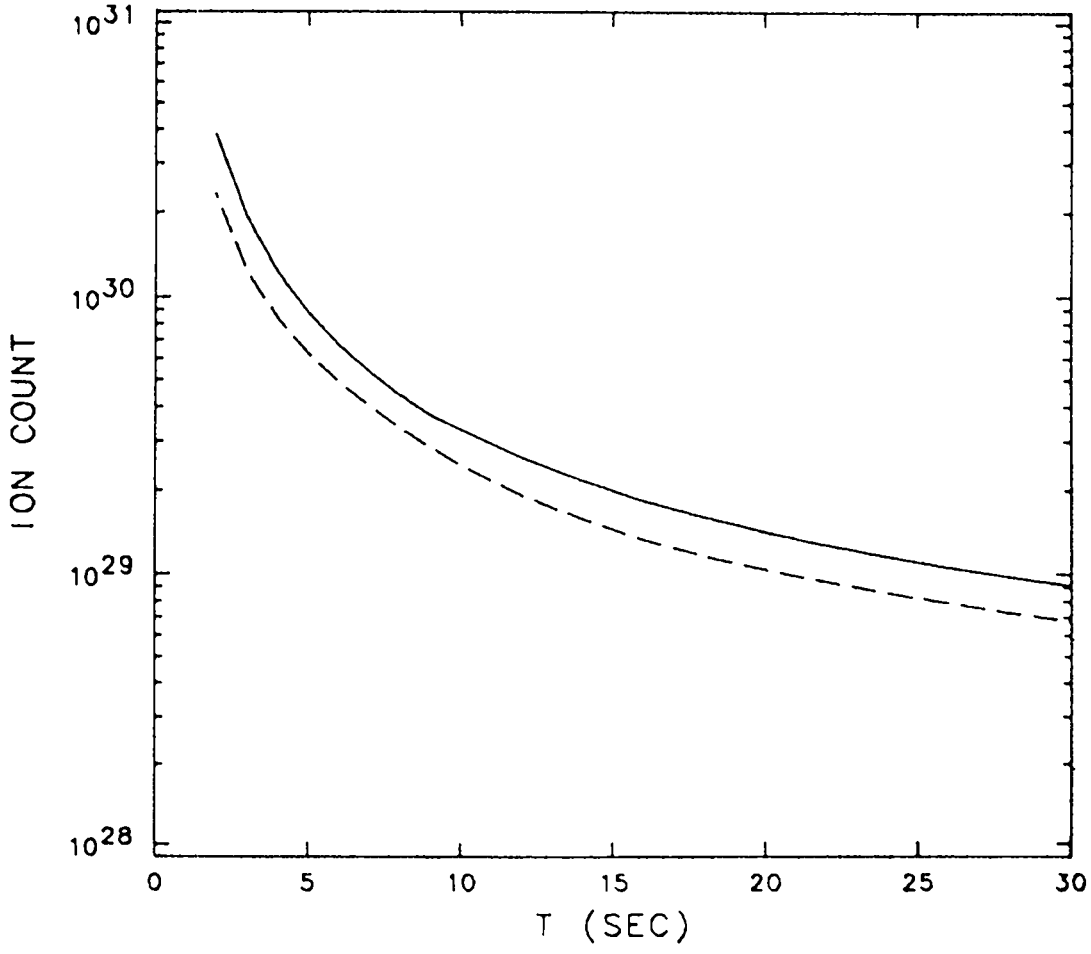

Fig. 4.4. The time evolution of the total number of ions in the computational grid for events 1 (dash) and 2 (solid). The number of ambient ions at this altitude is negligible.

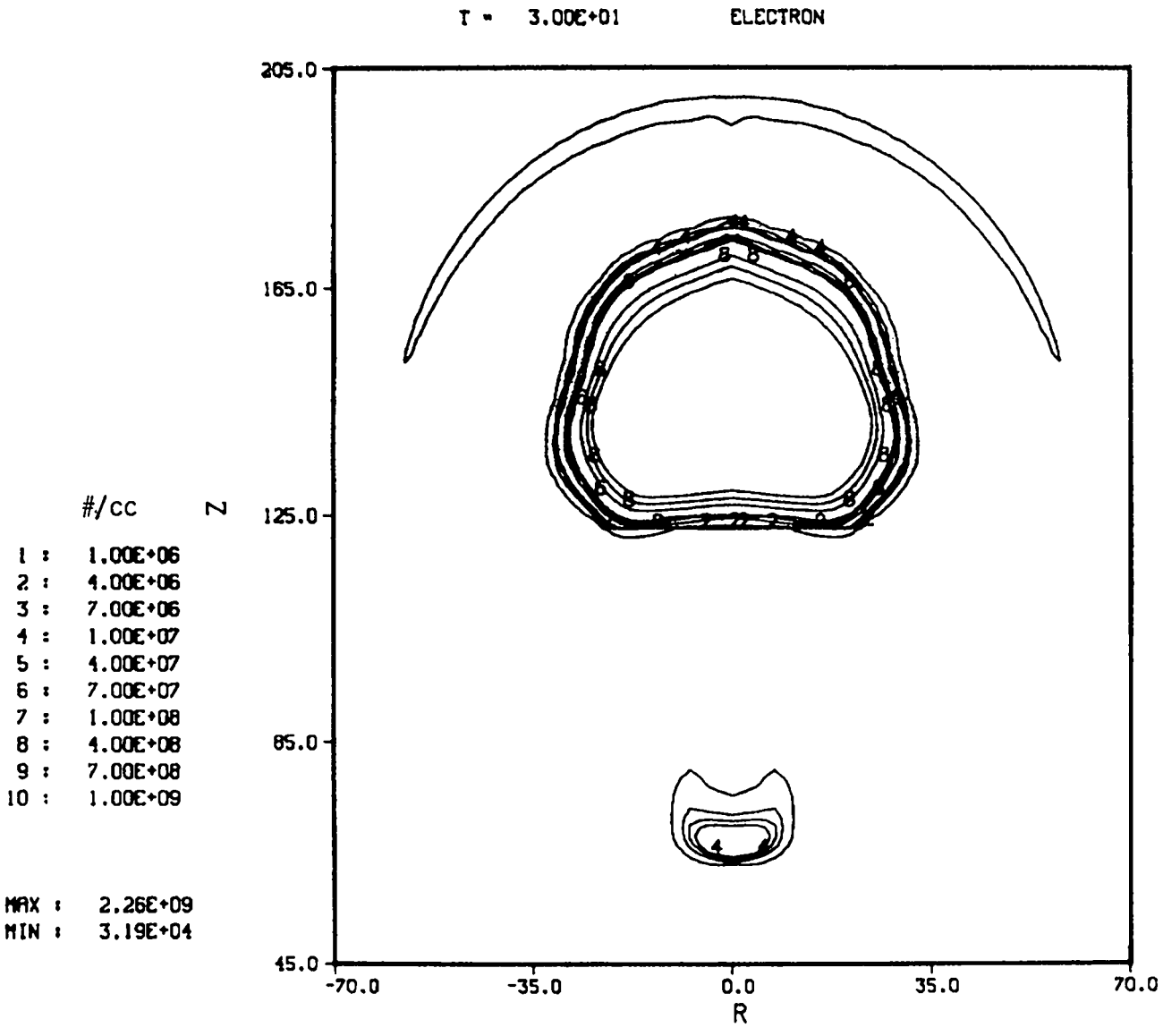

Fig. 4.5.a. Contours of constant electron density (number/cc) for event 2. We see three regions of high electron concentration.

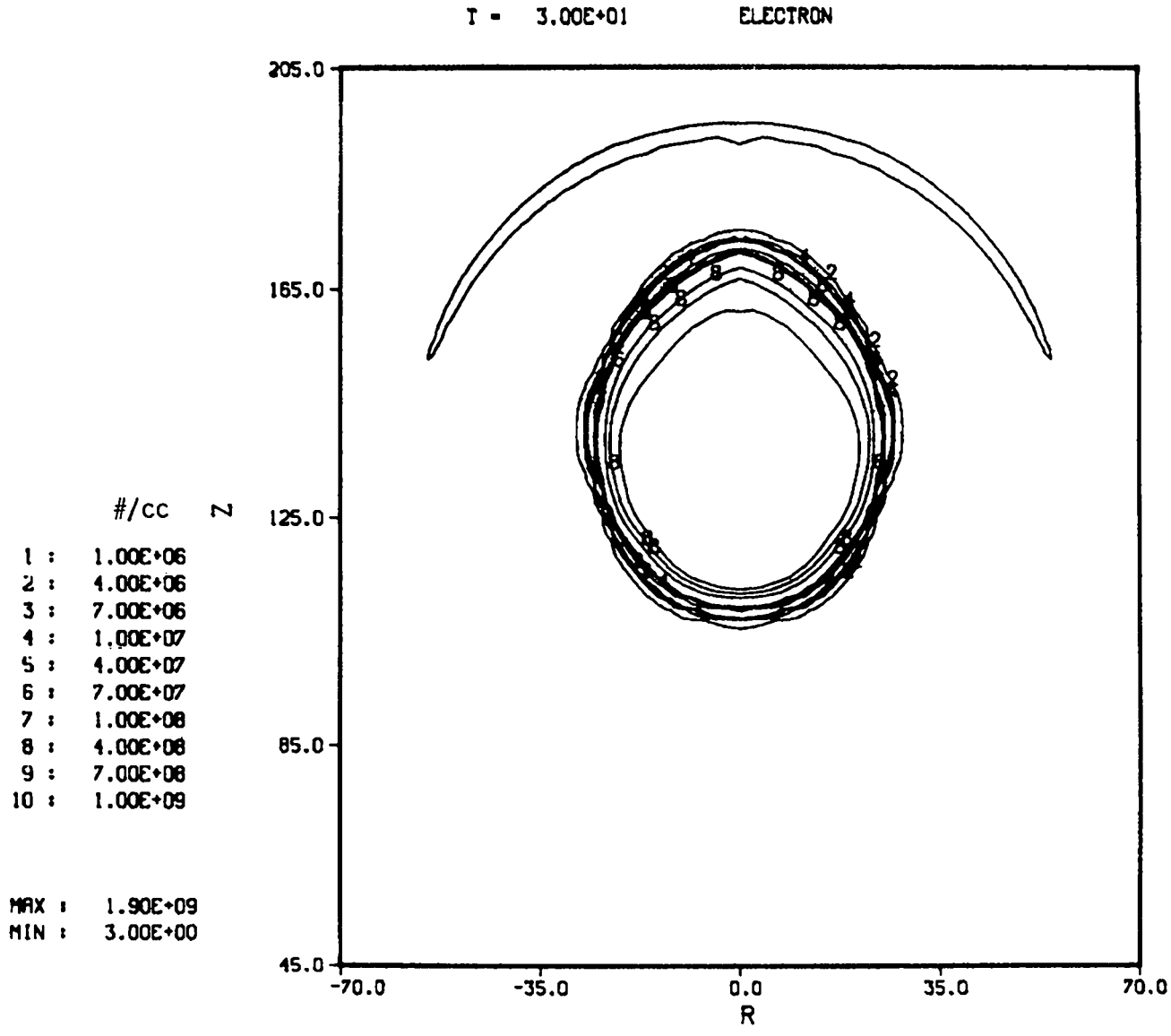

Fig. 4.5.b. Contours of constant electron density for event 1. The grid scales and the contour levels are identical to Figure 4.5.a. We see two regions of high electron concentration.

The heave of the disturbed air is an important aspect of fireball evolution because it moves substantial mass to higher altitudes for long periods of time. Figures 4.6.a,b plot contours of constant density, at 30 s, for events 2 and 1 respectively. The higher altitude contour levels 1–6 are very similar in shape and location for the two events. In fact, the $5 \times 10^{-11} gm/cc$ density layer is heaved 45 km, at the vertical symmetry axis, for both events. The $1 \times 10^{-9} gm/cc$ density layer is heaved only 6.5 km for event 1, but 20 km for event 2. The lower burst in event 2 enhances the heave of the middle density layer contours seven and eight, enhances the downward push of the lower layer contours 11 to 14, and complicates the shapes of the contours 9 and 10. For example, the $1 \times 10^{-7} gm/cc$ layer is depressed 5 km in event 1 and is depressed approximately twice that much for event 2.

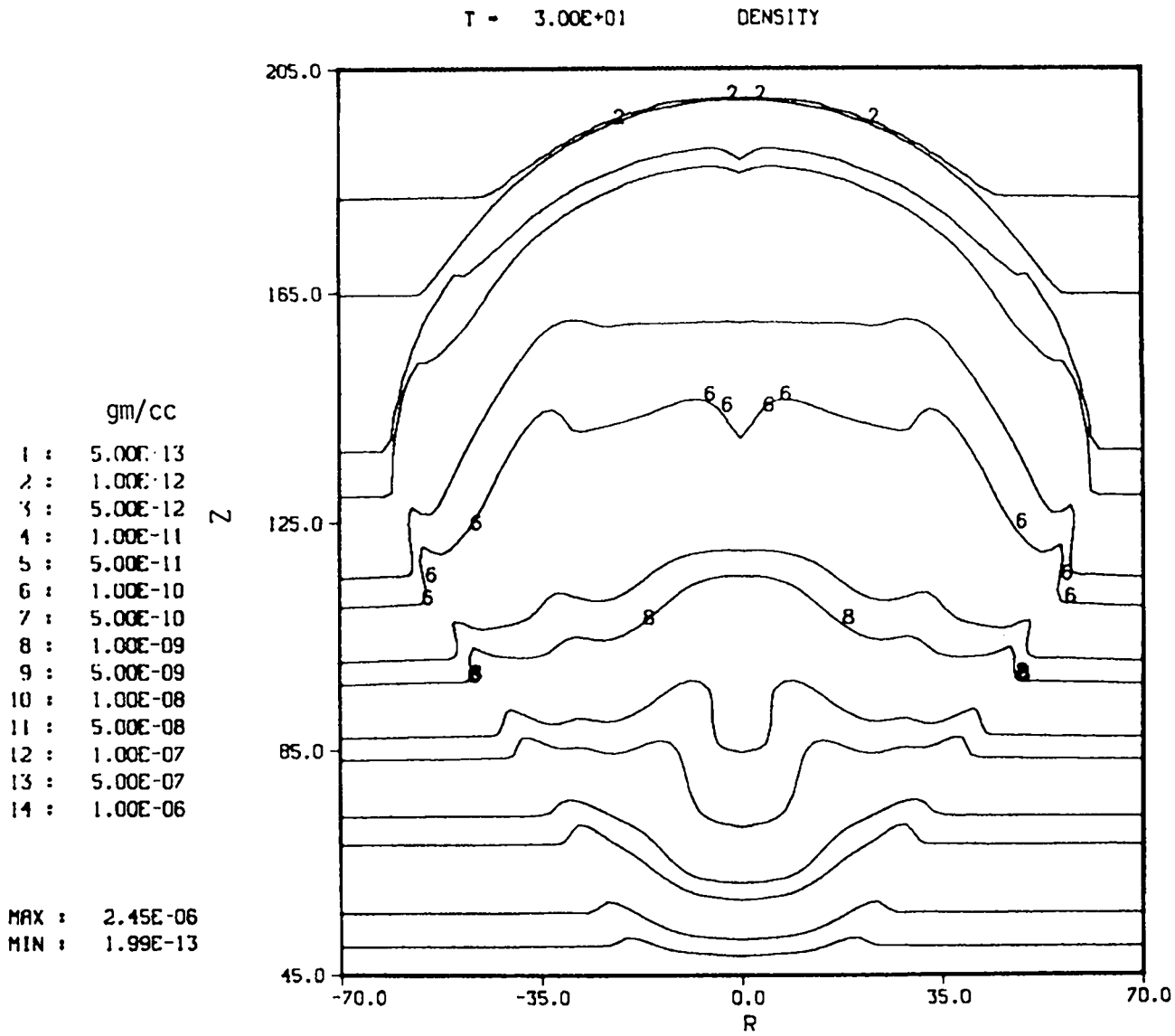

Fig. 4.6.a. Contours of constant mass density (gm/cc) for event 2.

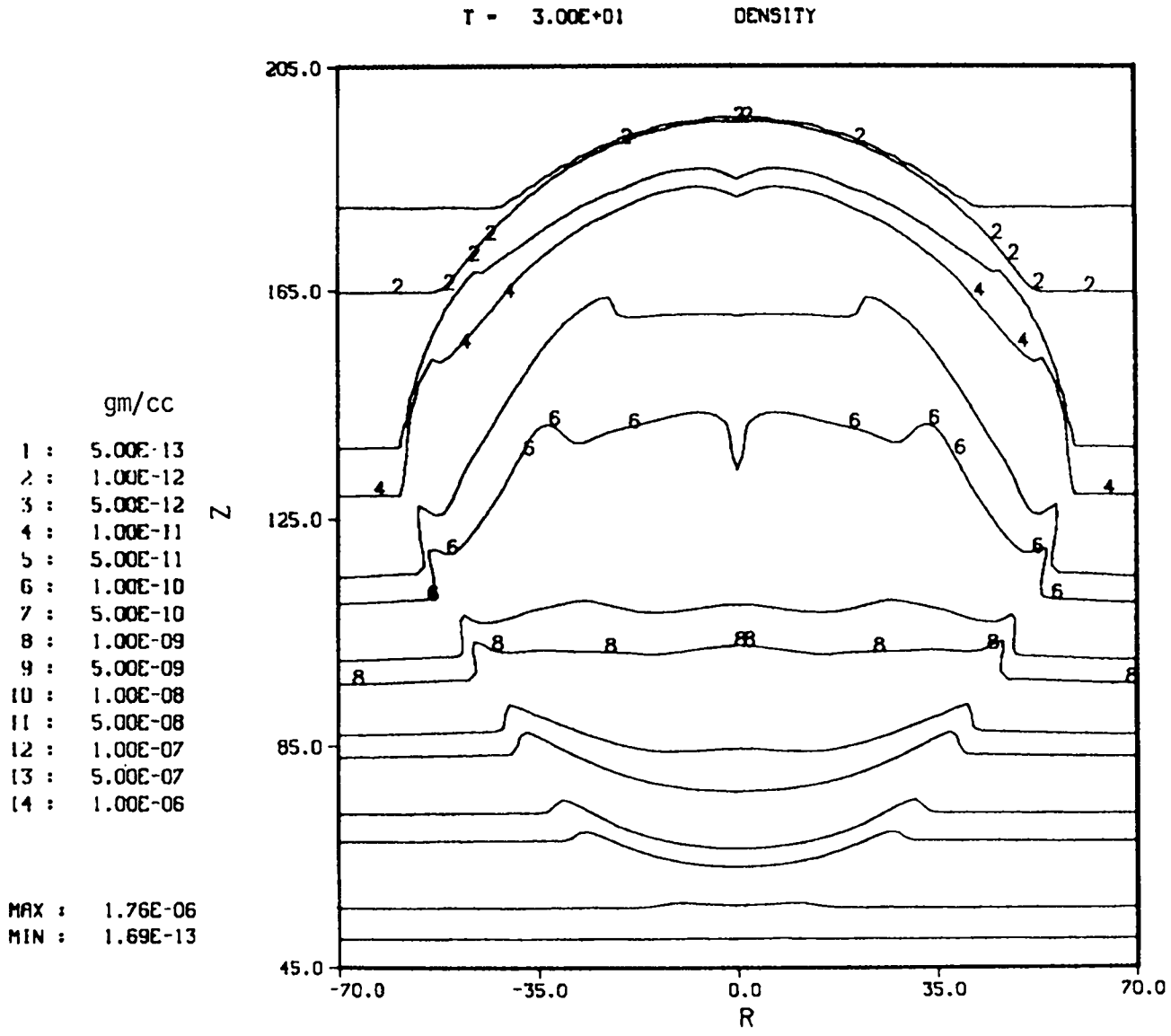

Fig. 4.6.b. Contours of constant mass density for event 1. The grid scales and the contour levels are identical to Figure 4.6.a.

VI. SUMMARY

We have described in detail the physics and chemistry modeling that is in FADCAT. The explicit, finite differenced, control volume hydrodynamics is exactly that of CAVEAT which is documented elsewhere. We have detailed the numerics of the inline chemistry model and have included the results from representative test cases. The chemistry modeling is an evolving process. This is because air chemistry is strongly altitude dependent and computationally time consuming. We have highlighted the results of two realistic burst scenarios.

The total computational grind time, on a CRAY XMP machine, for the two events simulated averaged out to be about 280 microseconds/zone/cycle which includes cpu, i/o, and memory. Since these simulations were run in the Lagrangian mode, with only an occasional remap, most of the cpu time was spent doing chemistry.

VII. APPENDIX A: ASPECTS OF THE NUMERICAL SOLUTION

In this section we describe the adaptations made to CAVEAT to create FADCAT. The key features of CAVEAT that made it useful for adaptation is: (1) its use of a Riemann solver and hence no need for artificial

viscosity, (2) its separation into a Lagrangian and rezone phase, (3) its second order spatial accuracy, and (4) its arbitrary Eulerian-Lagrangian (ALE) mode of operation option. The term rezone means here the advection done every hydrodynamic cycle in a non-Lagrangian simulation. The hydrodynamic motion of a fireball is dominated by its high Mach number shock front. The Riemann solver, coupled with the second order spatial accuracy, provides exceptional shock resolution without the adjustable parameters that would be necessary in an artificial viscosity formulation. Also, the Riemann solver naturally leads to defining all physical variables at cell centers. This is especially useful because then only one volume element is involved when calculating energy sums for an energy conservation check. In fact, when gravity is ignored, FADCAT conserves total energy to machine accuracy.

The in-line chemistry, discussed in an earlier section, assumes that it is operating on a Lagrangian volume element. In other words there is no species influx from neighboring cells. It is therefore called at the end of the Lagrangian phase of the hydrodynamics. If the particular evolution is not run purely Lagrangian, then the number densities and vibrational energy (instead of mass density in a purely hydro calculation) are advected in the rezone phase. At the end of the rezone phase the cell temperatures are adjusted to satisfy Equation 3.11.

FADCAT is usually run in a purely Lagrangian mode, with an occasional remap to an entirely new computational grid. The term remap means the mapping of the code variables into a new arbitrary grid. This is only done when the current grid is inadequate due to, for example, distortion. However, this requires a careful observance of zonal geometries and usually results in the smallest timestep relative to other possible modes. Therefore we sometimes run in an almost Lagrangian mode. In this mode the grid vertex velocities are a linear combination of the Lagrangian vertex velocities and the rezone vertex velocities. Rezone velocities can be determined by a variety of techniques. The scheme of Brackbill and Saltzman [18] is a notable method that is used in CAVEAT. This technique uses the mesh generator equations so that adaptivity in the mesh motion can be included. Also for some problems, and for some time intervals, it is advisable to run in an Eulerian mode. An example is the case of multiple interacting bursts, or bursts where vortex motion is extreme.

One of the fireball adaptations made to CAVEAT is the installation of a conservative remap, mentioned in section 2, for doing the occasional remap to an entirely new grid. We have chosen to conserve total energy (excluding gravitational), mass, and momenta. There is, therefore, some exchange between kinetic and internal energies. Gravitational energy is also not conserved because it depends on the mass distribution and not just the mass.

We also evolve, in FADCAT, a set of massless Lagrangian markers. The number of markers and their initial distribution $\mathbf{x}_m^0$ is determined by some problem dependent criterion. Their evolution is then followed by

$$\mathbf{x}_m(t) = \mathbf{x}_m^0 + \int_0^t \mathbf{u}_p \, dt$$

where $\mathbf{u}_p$ is the velocity at the position of the marker as a function of time. Marker output includes the initial number densities at each marker, and the density, temperature, and position of each marker as a function of time. The marker position is updated every computational cycle, which means the marker must be located to within a particular cell every cycle. This location is done by means of a a very efficient locator routine written by J.U. Brackbill [19]. Full marker data is output at a pre-determined, problem dependent set of times. Figure A.1 displays the time evolution of $\mathbf{x}_m$ (i.e. r and z in cylindrical geometry), the temperature, and the density for a typical run.

We have implemented these markers for chemical post-processing. Post-processing is necessary for emission estimates of the fireball. It involves doing detailed chemistry on the marker output. Detailed chemistry solves a network consisting of several hundred reactions and numerous species. The exact species set and the corresponding set of reactions is problem dependent. The detailed chemistry involves the numerical solution of a set of ordinary differential equations of the form:

$$\frac{d[n_i]}{dt} = P_i(t,[n_i]) - L_i(t,[n_i]) + [n_i]\frac{\delta ln\rho}{\delta t}$$

The term $[n_i]\frac{\delta ln\rho}{\delta t}$ describes the change in species n_i due to volume change. The factor $\frac{\delta ln\rho}{\delta t}$ in this term is evaluated at each interval between FADCAT marker output times. The terms P_i and L_i are rates of production and loss, respectively, by chemical kinetics for species n_i . These terms are sums over all the reactions in which species n_i is involved as a product or reactant species, respectively. The terms in each sum are the product of the rate constant times the product of the concentrations of all reactants in the reaction. The rate constants involved are functions of the temperature, and are evaluated whenever the FADCAT temperature varies by a prescribed factor. The initial concentrations are set to those used by FADCAT for the FADCAT species at the initial marker locations, and to zero for other species.

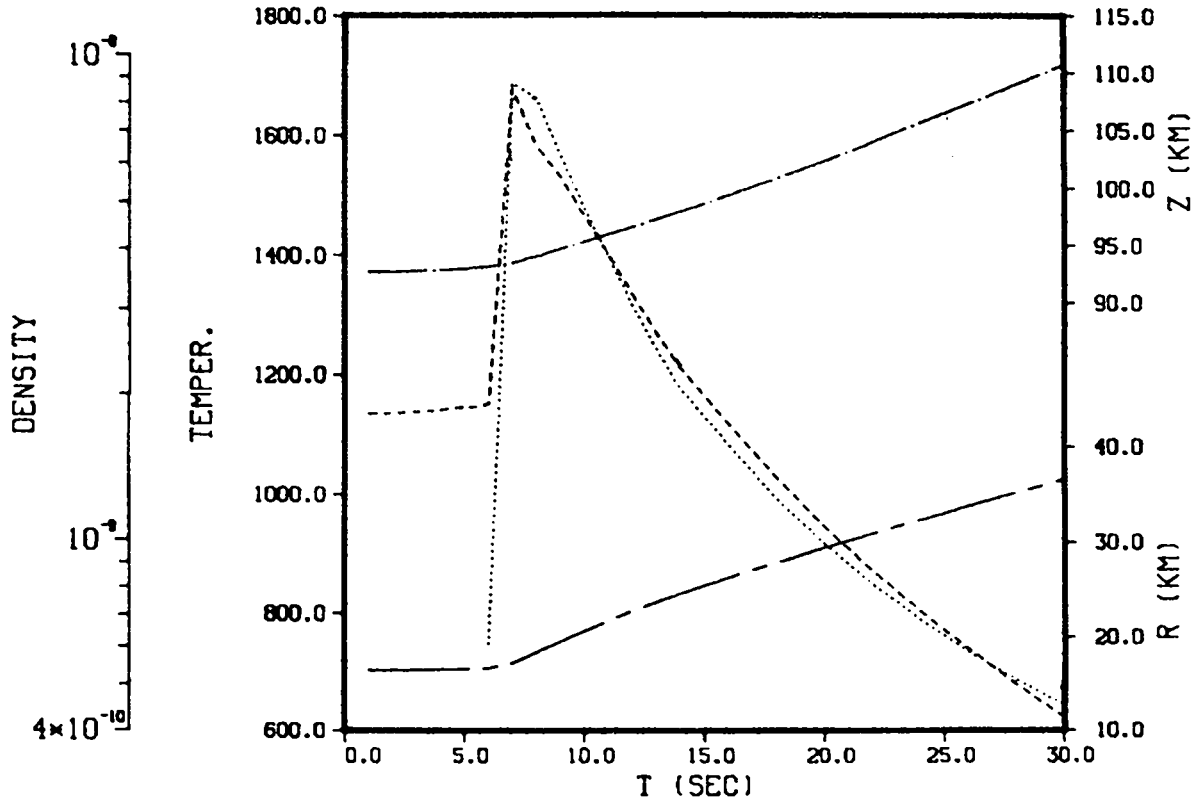

Fig. A.1. The marker output from a typical run. In this case, marker 1691 had an initial position of about 16 km in radius (chain dash) from the burst point and was about 13 km above the burst point of 80 km (chain dot). The marker was first hit by the shock, emanating from the fireball, at about 6 seconds. The temperature (dot) of the marker quickly rose to about 1700 K and cooled thereafter. The density (dash) quickly quadrupled and then decreased by a factor of about 16 by a time of 30 seconds.

REFERENCES

1. F.L. Addessio, D. E. Carroll, J. K. Dukowicz, F. H. Harlow, J. N. Johnson, B. A. Kashiwa, M.E. Maltrud, and H. M. Ruppel, *CAVEAT: A Computer Code for Fluid Dynamics Problems with Large Distortion and Internal Slip*, Los Alamos Nat. Lab. Report LA-10613-MS, 1986.

2. U.S. Standard Atmosphere 1962 U.S. Government Printing Office, Washington, D.C., 1962.

3. CIRA 1965 COSPAR International Reference Atmosphere 1965, COSPAR Working Group IV, North Holland Publishing Co.-Amsterdam, 1965.

4. J. Hilsenrath, M. Klein, and H. W. Woolley, *Tables of Thermodynamic Properties of Air Including Dissociation and Ionization from 1500 K to 15000 K*, NBS Report AEDC-TR-59-20, December 1959.

5. J. Hilsenrath, M. G. Green, and C. W. Beckett, *Thermodynamic Properties of Highly Ionized Air*, AFSWC report SWC-TR-56-35, April 1957.

6. F. R. Gilmore, *Equilibrium Composition and Thermodynamic Properties of Air to 24000 K*, Rand Corp. memorandum RM-1543, August 1955.

7. J. K. Dukowicz and J. W. Kodis, *Accurate Conservative Remapping (Rezoning) for Arbitrary Lagrangian Eulerian Computations*, **SIAM J. Sci. Stat. Comput.** May 1987.

8. J. K. Dukowicz, *A General Non-Iterative Riemann Solver for Godunov's Method*, **J. Comput. Phys.**, 61:119-137, 1985.

9. W. Lotz, *Ap.J. Supplement Series* **128**, Vol XIV, p. 207-238 (1967).

10. The rate constants are computed with the technique described by D.R. Bates, A.E. Kingson, and R.W.P. McWhirter, *Proc. Roy. Soc.* **A267** 297 (1962). Details of the application to oxygen are given in D.S. Sappenfield, DASIAC Nuclear Weapons Effects Review 66-3 (DASA 1825) p7 (CRD).

11. **Defense Nuclear Agency Reaction Rate Handbook**, M.H. Bortner and T. Baurer,eds., Defense Nuclear Agency report DNA 1948H (March 1972).

12. M. McFarland, D.L. Albritton, F.C. Fehsenfeld, E.E. Ferguson, and A.L. Schmeltekopf, *J. Chem. Phys.*59, 6620 (1973).

13. From detailed balance.

14. NASA panel for Data Evaluation, *Chemical Kinetics and Photochemical Data for Use In Stratospheric Modeling*, W.B. Demore, chairman, Jet Propulsion Laboratory report 83-62 (September 1983).

15. Forward rate constant from Ref. 3. Reverse rate constant by detailed balance.

16. C.W. Gear,**Numerical Initial Value Problems in Ordinary Differential Equations**, Prentice Hall, 1971.

17. S. Glasstone and J. Dolan, **The Effects of Nuclear Weapons**, third edition, 1977.

18. J. U. Brackbill and J. S. Saltzman, *Adaptive Zoning for Singular Problems in Two Dimensions*, **J. Comput. Phys.**, 46:342,368 (1982).

19. J. U. Brackbill and H. M. Ruppel, *FLIP: A Method for Adaptively Zoned, Particle-in-Cell Calculations of Fluid Flows in Two Dimensions*, **J. Comput. Phys.**, 65:314,343 (1986).

20. J. Zinn, *A Finite Different Scheme for Time-Dependent Spherical Radiation Hydrodynamics Problems*, **J. Comput. Phys.** 13:569 (1973).

Printed in the United States of America
Available from
National Technical Information Service
US Department of Commerce
5285 Port Royal Road
Springfield, VA 22161

Microfiche (A01)

Page Range	NTIS Price Code
001-025	A02
026-050	A03
051-075	A04
076-100	A05
101-125	A06
126-150	A07
151-175	A08
176-200	A09
201-225	A10
226-250	A11
251-275	A12
276-300	A13
301-325	A14
326-350	A15
351-375	A16
376-400	A17
401-425	A18
426-450	A19
451-475	A20
476-500	A21
501-525	A22
526-550	A23
551-575	A24
576-600	A25
601-up*	A99

*Contact NTIS for a price quote.